UNIVERSIDAD TÉCNICA FEDERICO SANTA MARÍA
DEPARTAMENTO DE FÍSICA
VALPARAÍSO - CHILE

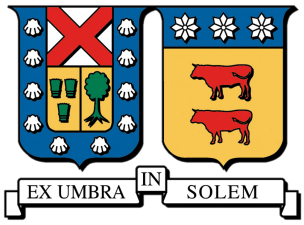

Two-Pion Bose-Einstein Correlation measurements with CLAS detector

Antonio Radic Brito

Contents

Abstract

In this analysis, we studied Bose-Einstein correlations for positive pions produced in DIS events. The analysed data came from experiments carried out during the run period EG2 in Jefferson Lab, Virginia. Multiple nuclear targets exposed to a 5.014 GeV electron beam. The studied nuclear targets were D2, C, Fe and Pb.

This phenomena has been studied in various types of scattering experiments such as pp, $\overline{p}p$, πp, Kp, e^+e^-, heavy-ion collisions, DIS, among others, measuring different kind of bosons, such as pions, kaons and photons. The HERMES collaboration using nuclear targets from ${}^1H$ to Xe found no significant variation among them.

By comparing the pairs of π^+ to uncorrelated pairs, we can obtain information of the space-time structure and dynamics of the source of the produced bosons. The goal of the study was to measure the size of the π^+ production source and its degree of coherence in one and two-dimensional approaches. A correlation function was constructed for each target by the ratio of the distribution of π^+ pairs, coming from a single event to a distribution of uncorrelated pairs. The uncorrelated pairs were constructed using an event-mixing method that takes pions from two different events.

The correlation function was corrected with a double ratio technique, using reconstructed events from simulations. By this way, biases from the experiment and analysis were removed from the correlation function.

The corrected correlation function was fitted by a Goldhaber parametrization in order to measure parameters of interest r and λ, which represent the size of the pion source and its degree of coherence respectively. No significant differences were found, regarding the size of the source along solid targets.

In the two-dimensional study, we obtained the parameters r_t and r_l. These represent

the size of the pion source along two perpendicular directions in order to measure a possible elongation of the source. Clear elongation was found for all nuclear targets with dependence in nuclear number A. Bigger elongation was found in light targets and it presented saturation for heavier targets, such as, Fe and Pb.

Chapter 1

Introduction

High energy physics experiments study the fundamental laws of the universe, and particularly, the microscopic structure of nuclear matter. Deep inelastic scattering (DIS) of lepton off a nucleon is a type of a particle experiment which may serve as an excellent tool for studies of hadron formation processes inside a nuclear medium. One of the phenomenas, which may play a fundamental role in the formation of those hadrons, are so-called Bose-Einstein correlations.

Bose-Einstein correlations (BEC), whose equivalent in astronomy is called Hanbury-Brown and Twiss effect , arises from the quantum mechanical interference between the symmetrized wave functions of identical bosons. This principle was first studied in radio astronomy by Hanbury Brown and Twiss to determine the spatial extent of photon radiating sources to measure stellar radii [1].

In the field of particle physics, this phenomenon was first observed in $\overline{p}p$ annihilations by G. Goldhaber, S. Goldhaber, W. Lee and A. Pais [2] [3].

This technique has been applied in various types of scattering experiments such as pp [4] [5] [6]; $\overline{p}p$, πp, Kp, e^+e^- [2] [7]; heavy-ion collisions [8] [9] [10] [11] [12], deep-inelastic lepton scattering [13] [14] [15]; among others, measuring different kind of bosons, such as pions, kaons and photons.

Two-pion Bose-Einstein correlations have been used in high energy physics experiments to obtain information about the space-time structure and the dynamics of the boson source, such as the shape and the size of the source.

Most of the scientific research, and as a consequence the theoretical knowledge on BEC comes from heavy-ions collision experiments. In those theories BEC is explained by a "fireball" [16] created in the collision considered as the source distribution that decay into hadrons, a process mostly described by hydrodynamics models. There are few works that consider the case of DIS and describe this phenomenon in terms of string-fragmentation models.

In this work, BEC were studied for positive pions produced in $e^{-}p$ interactions in the DIS regime using multiple nuclei targets from deuterium to lead in order to observe possible nuclear dependence. We measured the size and shape of the pion source and its degree of coherence.

The formation process of hadrons after a quark is struck by the lepton can extend beyond the nuclei. Interactions with the struck quark or the formed hadrons with the medium could alter the measured size and the coherence of the formation zone. The Big Bubble Chamber Neutrino Collaboration (BBCNC) studied Bose-Einstein correlations in neutrino and antineutrino interactions with nucleus and found no substantial differences between the data obtained from ^{1}H, ^{2}H and Ne [17]. The HERMES collaboration using nuclear targets from ^{1}H to Xe found no significant variation among them. [14].

1.1 Bose-Einstein Correlation

1.1.1 Definition

In classical mechanics, where we can describe a particle's position and movement with total certainty, we can track two identical particles and distinguish them, and follow their trajectories. Contrary to classical mechanics, in quantum mechanics, identical particles are indistinguishable and we can not track their trajectories at any time. One of its basic principles in the quantum theory is that particles and systems composed of multiple particles can be described mathematically with wave functions. We can describe a system of n identical particles as $\Psi_n(q_1, ..., q_i, ..., q_j, ...q_n)$, where q_i indicate the coordinates that describe particle i. We can apply a permutation operator P_{ij} on the

wave function of the system, which swap the position of particles i and j. If we apply the same P_{ij} twice, the wave function Ψ will remain the same. Therefore $P_{ij}^2\Psi = \Psi$, and its eigenvalues are $+1$ and -1. The wave function Ψ will be completely symmetrical or asymmetrical. In the case of completely symmetrical wave functions the particles are called bosons. On contrary, they are called fermions.

In order to study the Bose-Einstein correlation we define a function for two-particles in the following way: the ratio of the two particle inclusive cross section to the product of the single-particle cross sections:

$$R_{(p1,p2)} = \frac{D(p_1, p_2)}{D(p_1)D(p_2)} \tag{1.1}$$

where p_1 and p_2 are the four-momenta of the particles, and $D(p_1, p_2)$, $D(p_1)$, $D(p_2)$ are the two-particle and one-particle probability densities.

We will find later that the correlation R will depend on the Lorentz-invariant quantity $Q_{12} = (\sqrt{-(p_1 - p_2)^2})$; the absolute value of the 4-momentum difference between the produced pair of particles, which will result on an enhancement on the pion production at low values of Q_{12}, which will show up as a bump in the correlation function's shape. Typically, the Goldhaber parametrization [3] -presented later in this thesis- is used to fit the correlation function obtained, so we can obtain quantities of interest.

1.1.2 Derivation of Bose-Einstein Correlation

In a quantum process, the probability of producing new particles is determined by the amplitude of the sum's square of multiple terms in the wave-function that contribute to the process. The sum's square will lead to interference terms that could enhance the total probability.

In order to understand the origin of Bose-Einstein correlations, we can start considering the most basic example presented in [18] and [14], two identical bosons, for instance, positive pions coming from two different point sources. We take the situation shown in Fig. 1.1 where two identical pions are emitted from the same event in the points r_1 and r_2 and detected at the detectors D_A and D_B with momenta k_A and k_B respectively. Both pions are identical and indistinguishable. Therefore, it is impossible

to determine which particle reached which detector. Because of their indistinguishability and combined with the fact that pions are bosons, the pions wave function must be symmetric under the exchange of them:

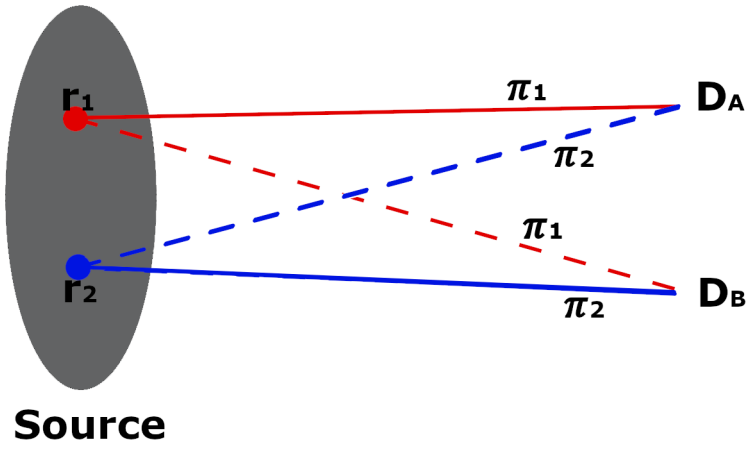

Figure 1.1: Scheme of Bose-Einstein correlation effect. Two identical pions are created in points r_1 and r_2 and detected in detectors D_A and D_B. Two possible scenarios are possible, represented by full lines and dashed lines.

$$\Psi_{A,B}(1,2) = \frac{\Psi_{1A}\Psi_{2B} + \Psi_{1B}\Psi_{2A}}{\sqrt{2}} \tag{1.2}$$

where Ψ_{1A} is the wave function of a pion produced at point r_1 with momentum k_A and detected at detector A . Assuming that both pions can be described by plane waves in the form $\Psi_{1A} \propto e^{ik_A r_1}$, the wave function of this process is given by:

$$\Psi_{k_A,k_B}(1,2)) = \frac{1}{\sqrt{2}}[e^{i(k_A r_1 + k_B r_2)} + e^{i(k_A r_2 + k_B r_1)}] \tag{1.3}$$

and the square of the wave function will have the following form:

$$|\Psi_{k_A,k_B}(1,2)|^2 = \frac{1}{2}[e^{i(k_A r_1 + k_B r_2)} + e^{i(k_A r_2 + k_B r_1)}][e^{-i(k_A r_1 + k_B r_2)} + e^{-i(k_A r_2 + k_B r_1)}] \tag{1.4}$$

$$|\Psi_{k_A,k_B}(1,2)|^2 = 1 + \frac{1}{2}[e^{i(k_A-k_B)r_1}e^{i(k_B-k_A)r_2} + e^{i(k_B-k_A)r_1}e^{i(k_A-k_B)r_2}] \tag{1.5}$$

We can rearrange this and get:

$$|\Psi_{k_A,k_B}(1,2)|^2 = 1 + \frac{1}{2}[e^{iq(r_1-r_2)} + e^{-iq(r_1-r_2)}] \tag{1.6}$$

and then we can obtain:

$$|\Psi_{k_A,k_B}(1,2)|^2 = 1 + cos(q(r_1 - r_2)) \tag{1.7}$$

This shows that the probability of the process and, therefore, the Bose-Einstein correlation effect depends on the spatial distance $(r_1 - r_2)$ between two particle sources and the momentum difference q between the observed pions.

The previous example considers the source of the pions as two points in space. In a more general case, if we consider that the pions are emitted from the whole source statistically independently with the density of the source represented as $\rho(r)$, we can get the total probability of the process integrating over r_1 and r_2, obtaining:

$$P_{k_1,k_2} \propto \int d^3r_1 d^3r_2 \rho(r_1)\rho(r_2)|\Psi_{k_A,k_B}(1,2)|^2 \tag{1.8}$$

$$P_{k_1,k_2} \propto \int d^3r_1 d^3r_2 \rho(r_1)\rho(r_2)(1 + \frac{1}{2}[e^{iq(r_1-r_2)} + e^{-iq(r_1-r_2)}]) = 1 + |\widetilde{\rho}(q)|^2 \tag{1.9}$$

where $q = k_1 - k_2$ and $\widetilde{\rho}$ is the Fourier transformation of $\rho(r)$.

Coherence Parameter

The previous treatment considers a complete chaotic source, but in reality, any degree of coherence can reduce the Bose-Einstein effect. In order to include the "phase" of each point-like oscillators, one can consider a time dependent amplitude $f(t)$ associated with each local source.

We can start by considering two point-like oscillators. The total amplitude for emitting a **single pion** with momentum k_A from those sources is given by:

$$\Psi_{k_A}(1,2) \propto [f_1 e^{ik_A r_1} + f_2 e^{ik_A r_2}] \tag{1.10}$$

where $f_1 = f_1(t)$ and $f_2 = f_2(t)$ represent the time dependence of the oscillators located at r_1 and r_2 respectively.

The probability for single particle production is obtained by squaring 1.10:

$$|\Psi_{k_A}(1,2)|^2 = [|f_1|^2 + |f_2|^2 + f_1\overline{f_2}e^{ik_A(r_2-r_1)} + f_2\overline{f_1}e^{ik_A(r_1-r_2)}]. \tag{1.11}$$

Now, the joint amplitude for a **two-pion** production process is given by the product of two single particle processes:

$$\Psi_{k_A,k_B}(1,2) = \Psi_{k_A}(1,2)\Psi_{k_B}(1,2) \propto [f_1 e^{ik_A r_1} + f_2 e^{ik_A r_2}][f_1 e^{ik_B r_1} + f_2 e^{ik_B r_2}] \tag{1.12}$$

And then we obtain the joint probability of the process by squaring 1.12:

$$\begin{aligned} |\Psi_{k_A,k_B}(1,2)|^2 =& [|f_1|^2 + |f_2|^2 + f_1 f_2^* e^{ik_A(r_2-r_1)} + f_2 f_1^* e^{ik_A(r_1-r_2)}]\times \\ & [|f_1|^2 + |f_2|^2 + f_1 f_2^* e^{ik_B(r_2-r_1)} + f_2 f_1^* e^{ik_B(r_1-r_2)}] \end{aligned} \tag{1.13}$$

In case of completely coherent sources, the amplitudes for radiation from each source do not change, and the product of both phases will simply be $< f_1 f_2^* >= f_1 f_2^*$ and $< f_2 f_1^* >= f_2 f_1^*$. The joint probability 1.13 in this particular case will take the form:

$$|\Psi_{k_A,k_B}(1,2)|^2_C = |\Psi_{k_A}(1,2)|^2 |\Psi_{k_B}(1,2)|^2 \tag{1.14}$$

and the correlation function disappear completely, in other words, the two-particle probability of detecting two identical pions will be equivalent to the product of two one-particle probabilities.

On the contrary, in case of completely incoherent sources, the amplitudes for radi-

ation from each source fluctuate wildly, and the average of the product of the phases $< f_1 f_2^* >=< f_2 f_1^* >= 0$. We can calculate the joint probability 1.13 easily considering all terms in the product containing: $f_1 f_2^*$, $f_2 f_1^*$, $(f_1 f_2^*)^*$, or $(f_2 f_1^*)^*$ are zero in average.

Then, the joint probability in the incoherent case is:

$$|\Psi_{k_A,k_B}(1,2)|_I^2 = (|f_1|^2+|f_2|^2)^2+|f_1|^2|f_2|^2[e^{i(r_1-r_2)(k_B-k_A)}+e^{-i(r_1-r_2)(k_A-k_B)}] \quad (1.15)$$

And we can obtain:

$$|\Psi_{k_A,k_B}(1,2)|_I^2 = (|f_1|^2 + |f_2|^2)^2 + 2|f_1|^2|f_2|^2 cos[(k_B - k_A)(r_1 - r_2)] \quad (1.16)$$

In this opposite case, the correlation function will be enhanced.

In order to clearly see the degree of enhancement, we can look at the definition of the correlation function $R_{(k_1,k_2)} = \dfrac{P(k_1,k_2)}{P(k_1)P(k_2)}$ which corresponds to the ratio of the two-particle probability densities divided by the product of two single particle distributions. We have: $P(k_1,k_2) =< |\Psi_{k_A,k_B}|^2 >$, $P(k_1) =< |\Psi_{k_A}|^2 >$ and $P(k_2) =< |\Psi_{k_B}|^2 >$,

Therefore, the correlation function in the coherent case will take the form:

$$R_{(k_1,k_2)C} = \frac{P(k_1,k_2)_C}{P(k_1)P(k_2)_C} = 1 \quad (1.17)$$

In the other hand, in the completely incoherent case:

$$R_{(k_1,k_2)I} = \frac{P(k_1,k_2)_I}{P(k_1)P(k_2)_I} = 1 + \frac{2|f_1|^2|f_2|^2 cos[q(r_1 - r_2)]}{(|f_1|^2 + |f_2|^2)^2} > 1 \quad (1.18)$$

We can notice that the correlation function $R_{(k_1,k_2)I} \rightarrow \dfrac{3}{2}$ when $q \rightarrow 0$, in the case both sources emitting with equal strength. When we add more sources [19], the

correlation function takes the form:

$$R_{k_1,\ldots,(k_n)I} \to 1 + (1 - \frac{1}{n}) \tag{1.19}$$

when $q \to 0$.

For a source with infinite emitters distributed over a region in space, the expression for the correlation function will take the form:

$$R(Q) = 1 + |\widetilde{\rho}(Q)|^2 \tag{1.20}$$

where $Q_{12} = (\sqrt{-(p_1 - p_2)^2})$ is the Lorentz invariant 4-momentum difference.

In reality, the emission region can be a mixture of coherent and incoherent sources. Such sources lead to intermediate cases which will manifest in the correlation function. To take into account this effect, a empirically factor λ was introduced. For a source with infinite emitters distributed over a region in space, the most general expression for the correlation function will take the form:

$$R(Q) = 1 + \lambda|\widetilde{\rho}(Q)|^2 \tag{1.21}$$

where λ is called chaoticity parameter. The chaoticity parameter λ shows the degree of coherence in the pion production. A completely coherent source ($\lambda = 0$) would show no interference, and $\lambda = 1$ corresponds to a complete incoherent source.

1.1.3 Goldhaber Parametrization

We have concluded that the Bose-Einstein correlation function depends on the density of the source; the 4-momenta difference between pions; and that it can show different grades of coherence. Regarding the pion source, we can assume a space-time distribution $\rho(r)$ proposed by Goldhaber corresponding to an emitting source with a spherical Gaussian density distribution:

$$\rho(r) = \rho(0)exp(\frac{-r^2}{2R^2}) \tag{1.22}$$

Considering this source distribution and using Eq. 1.21, we can obtain that the

Bose-Einstein correlation will have the following form, called Goldhaber parametrization:

$$R(Q_{12}) = (1 + \lambda exp(-r^2 Q_{12}^2)) \tag{1.23}$$

where the parameter r represents the size of the pion production zone and λ is the coherence parameter previously discussed. Different experimental effects could include final state interactions between the pions or misidentification of particle which leads to the reduction of the purity of the pion sample. These effects can modify the λ parameter below or over 1, which makes it difficult to compare measured values of λ between experiments.

1.1.4 Coulomb Correction

When we deal with charged particles, we have to consider the Coulomb force between them [20]. In Bose-Einstein correlations, we work with identical particles with the same charge so the repulsive Coulomb force tend to separate the pair and reduce the enhancement signal. In case of opposite charged particles, the effect is reversed when compared to the like-sign case, and particles tend to get closer. The measured distribution of pion pairs, including the effect of Coulomb interaction force, can be described as:

$$N_{measured}(Q) = G(Q)N(Q) \tag{1.24}$$

where $N_{measured}$ is the measured pair distribution, $G(Q)$ is the Coulomb correction factor, and $N(Q)$ is the pair distribution free of Coulomb force. The most simple expression for $G(Q)$ is the Gamow factor [19] given by:

$$G_l(\eta) = \frac{\eta}{exp(\eta) - 1} \tag{1.25}$$

$$G_u(\eta) = \frac{\eta}{1 - exp(-\eta)} \tag{1.26}$$

respectively -for like-sign and unlike-sign pairs- where $\eta = 2\pi\alpha m_\pi / Q$, α is the fine structure constant (1/137) and m_π is the particle mass. The intensity of this correction is shown in Fig. 1.2. The Gamow factor is calculated assuming that both particles

are created in single point -which is not the case in the Bose-Einstein correlations-. Therefore, this approach would not be optimal [21]. We can also consider that, at $Q_{12} = 0.05[MeV]$, the Gamow factor is only around 2% and its effect negligible. We decided not to include this correction in the analysis. Instead, we only considered for the final fit the range $Q_{12} > 0.05[MeV]$, as proposed in [14]. Below this point, the Coulomb effect are strong enough to be considered.

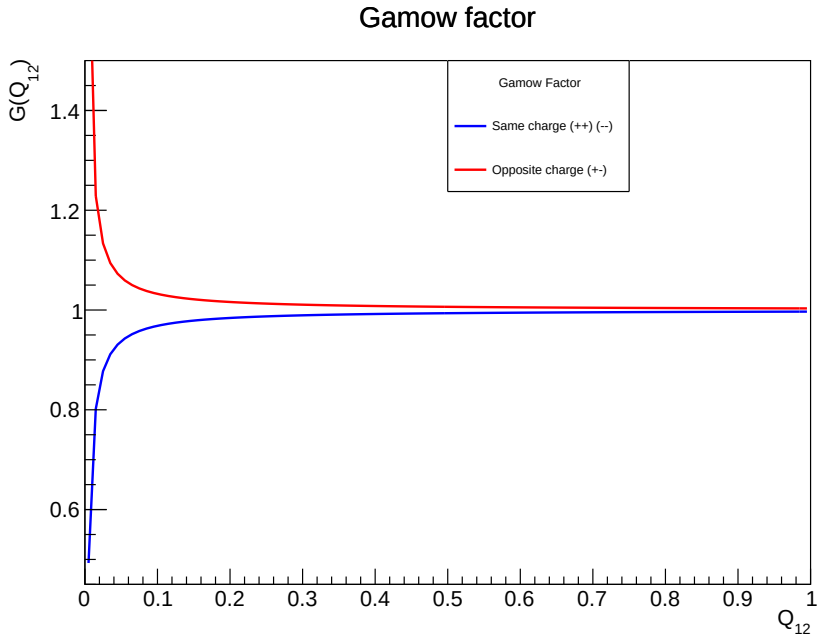

Figure 1.2: Gamow factor for like and unlike sign pairs. This factor is used to correct the measured distribution of detected pairs affected by Coulomb force.

Chapter 2

Experimental Setup

The experiments (E02-104, E02-110) were carried out during the run period called EG2, from January 9, 2004 to March 5, 2004, in the experimental Hall-B at Thomas Jefferson National Accelerator Facility, in Newport News, VA, USA. The electron beam from CEBAF (Continuous Electron Beam Accelerator Facility) is simultaneously delivered into three different experimental areas, which are Halls A, B and C. The main detector in Hall B was called CLAS (CEBAF Large Acceptance Spectrometer) [22], and it was designed to operate with both electron and photon beams of 5 GeV during the EG2 run period. A schematic of the facility, including the accelerator and the experimental halls, are shown in Fig. 2.1.

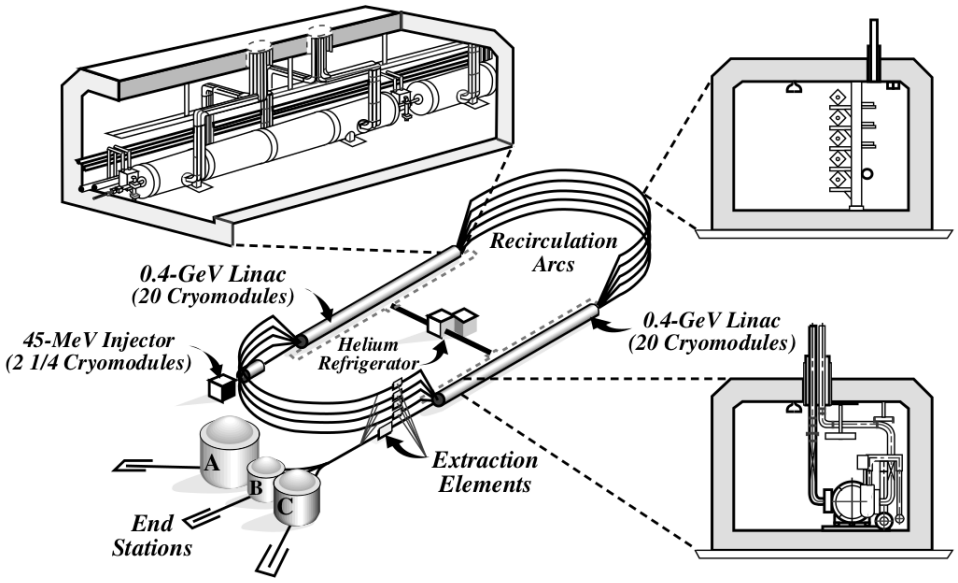

Figure 2.1: CEBAF accelerator and experimental halls.

2.1 CLAS

The CLAS design is based on a toroidal magnetic field. Such field provides the ability to measure charged particles with good momentum resolution and keep a zone around the target free of magnetic field which allows the use of dynamically polarized targets. The magnetic field is generated by six superconducting coils around the beam axis. The detection system is composed of Drift Chambers (DF) to determine trajectories of charged particles; Cherenkov Counters (CC) for electron identification; Scintillation counters (SC) for measuring time-of-flight (TOF); and electromagnetic calorimeters (EC) to measure particle energy and neutral particles as neutrons. All segments form six independent spectrometers with a common target, trigger and data acquisition. For electron scattering experiments, a small normal-conducting mini-torus surrounds the target to keep low momentum electrons produced by Møller scattering from reaching the innermost drift chambers. The schematic view of the detector with the beamline and the target region can be seen in Fig.2.2 and perpendicular to the beam in Fig. 2.3. A spherical coordinate system is used to describe the geometry of the experiment .The

z-axis is taken to lie along the beam direction with θ as the polar (scattering) angle, and ϕ as the azimuthal angle. The x and y directions are respectively horizontal and vertical in the plane normal to the beam.

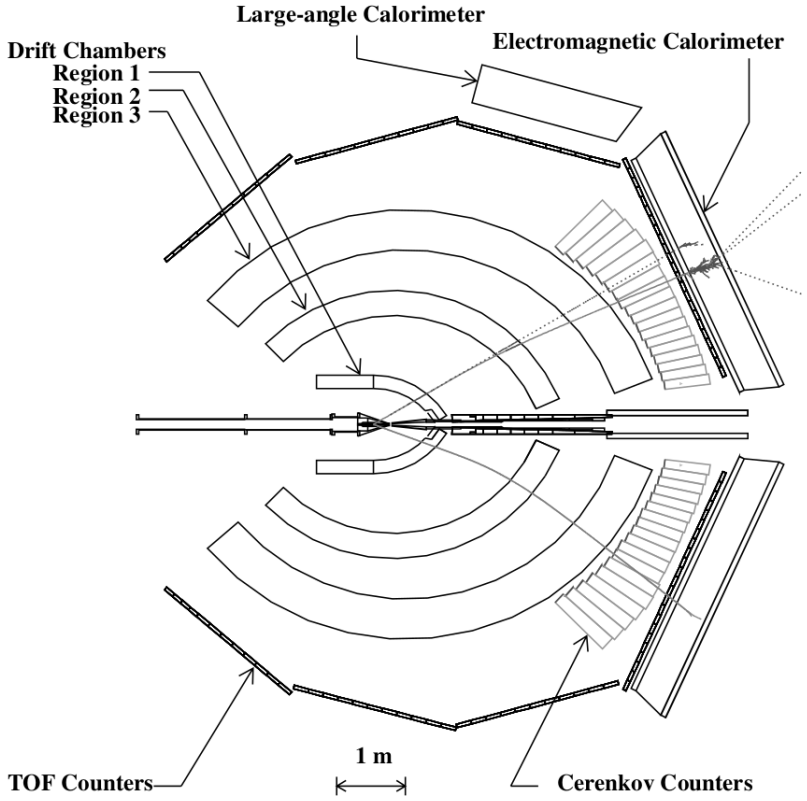

Figure 2.2: CLAS schematic along the beam line. Typical photon, electron and proton tracks from an interaction are illustrated.

2.1.1 Torus Magnet

The magnetic field for the momentum analysis of charged particles is generated by six superconducting coils arranged in a toroidal geometry around the electron beam line. The magnetic field can be calculated directly from the current in the coils because there is no iron in the system. The layout of the coils and contours of constant absolute field strength are shown in Fig. 2.4. The magnet is approximately 5 m in diameter and 5 m in

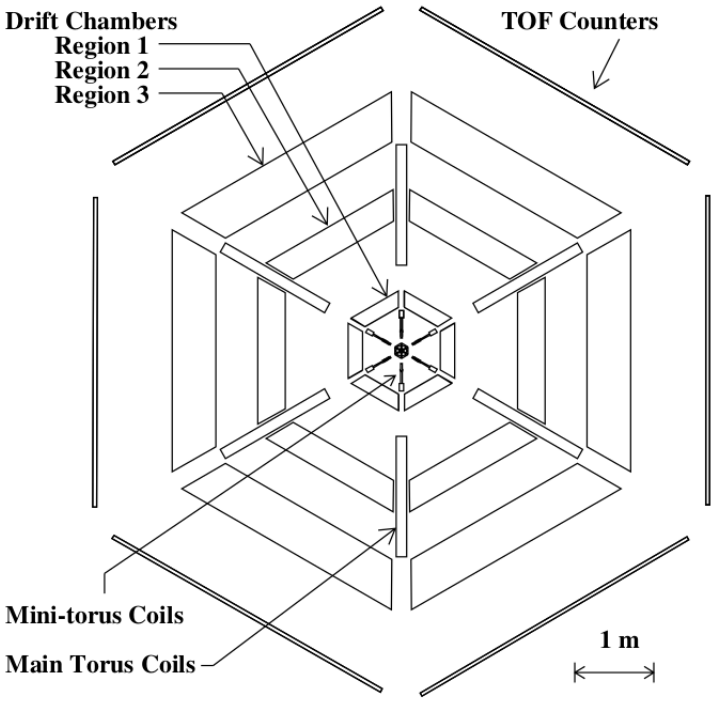

Figure 2.3: CLAS view in a plane perpendicular to the beam direction.

length. The main field component is in the ϕ-direction. However, there are significant deviations from a pure ϕ-field close to the coils. The effect of these deviations on the particle trajectories is minimized by the circular inner shape of the coil: particles coming from the target do not experience a significant deflection in ϕ when crossing the inner boundary of the coil. The magnet bends charged particles toward or away from the beam axis depending on the sign of the charge but leaves the azimuthal angle essentially unchanged.

2.1.2 Drift Chambers (DC)

The magnet coils separate the detector in six different areas or sectors. In each of the six sector, 18 separate drift chambers were grouped in 3 different radial regions. Each of these regions has different magnetic field intensities. The six "Region One" chambers are closer to the target in an area of low intensity field. The six "Region Two" chambers

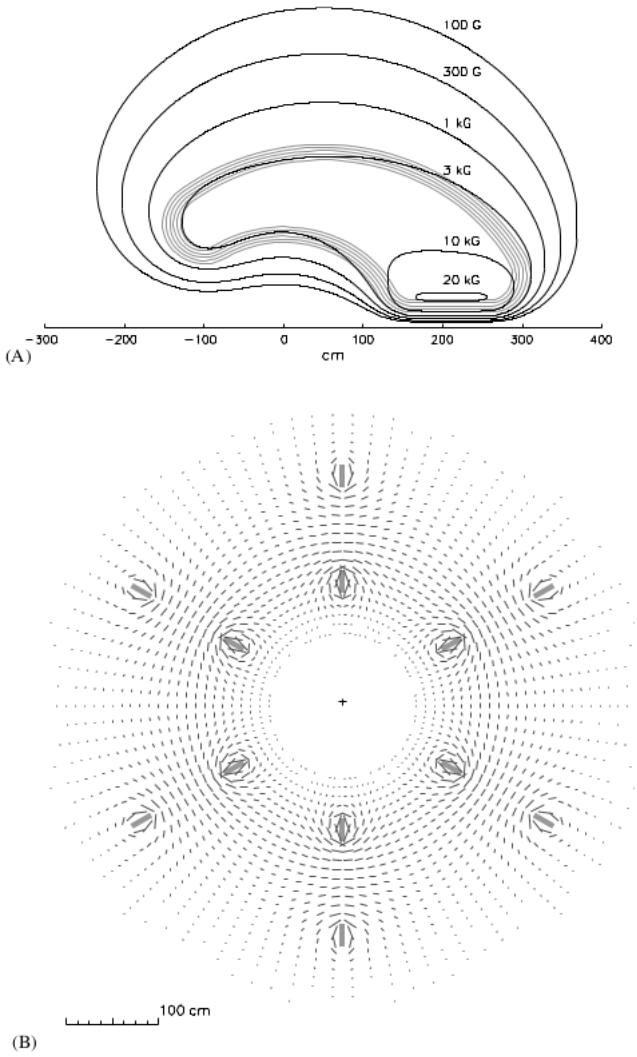

Figure 2.4: Magnetic field contour produced by the super conducting coils.

are placed between the magnet coils in an area of high intensity field near the point of maximum track saggita. And the six "Region Three" are located outside the magnetic coils.

The wires placed in the chambers were stretched between two endplates. Each parallel to its closest coil plane, and thus tilted at 60^o with respect each other. For pattern recognition and tracking redundancy, the wire layers in each chamber are grouped into

two superlayers of six wire layers each: one axial to the magnetic field, and the other tilted at a 6^o stereo angle to provide azimuthal information. The stereo superlayer of Region One is an exception to this rule, consisting of only four wire layers due to space constraints. The wire layout can be seen in Fig. 2.5.

From considerations of system safety, as well as in order to improve the operating lifetime, an 88–12% mixture of Ar and CO_2 was used.

Details on the drift chamber system can be found in [23].

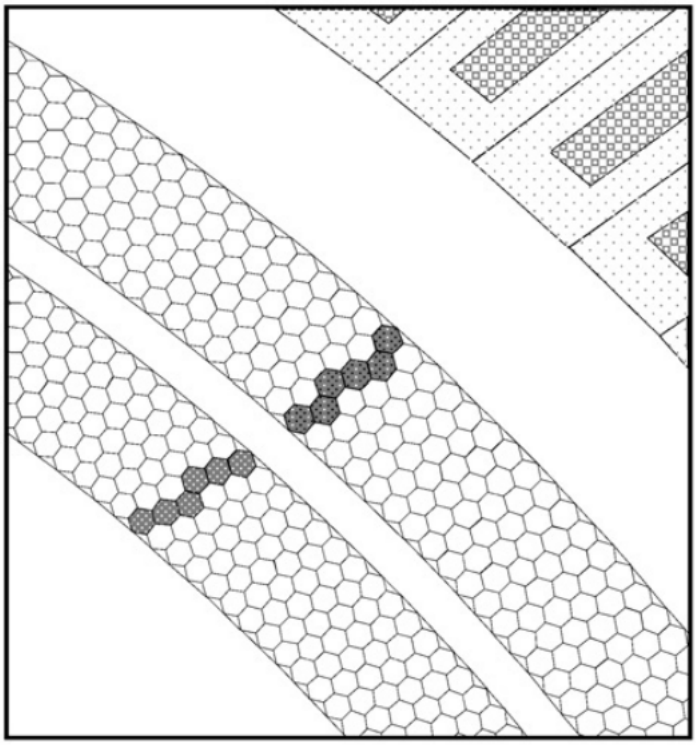

Figure 2.5: Representation of a Region Three chamber, showing the layout of its two superlayers. The sense wires are at the center of each hexagon and the field wires are located are the vertices. A passing particle is shown by the highlighted drift cells that have fired.

2.1.3 Cherenkov counters, CC

The Cherenkov Counters have two main functions: triggering electrons and discriminating pions from electrons. In each sector, CC covers out an angle of $\theta = 45^o$. Placing the light collecting and PMTs in the region of ϕ covered by the magnet coils and covering most the available space with mirrors as seen in Fig. 2.6, a low amount of material in the sensitive area is placed, preventing degradation of energy resolution. Since the charged particle trajectories lie in planes of constant ϕ, the placement of the PMTs does not affect the angular coverage. The light-collection optics were designed to focus the light only in the ϕ direction, which preserves the information on the electron polar angle θ. The PMTs were covered with high-permeability magnetic shields because they were located at the field's region of the torus with the highest transverse fields. The Cherenkov radiator gas, used in the detector, was perfluorobutane (C_4F_{10}) with a refractive index of 1.00153, which results in a pion momentum threshold of 2.5 GeV/c. An inbending electron, passing through the active volume of the detector, results in typically 4-5 photoelectrons.

Details on the CLAS Cherenkov detector can be found in [24].

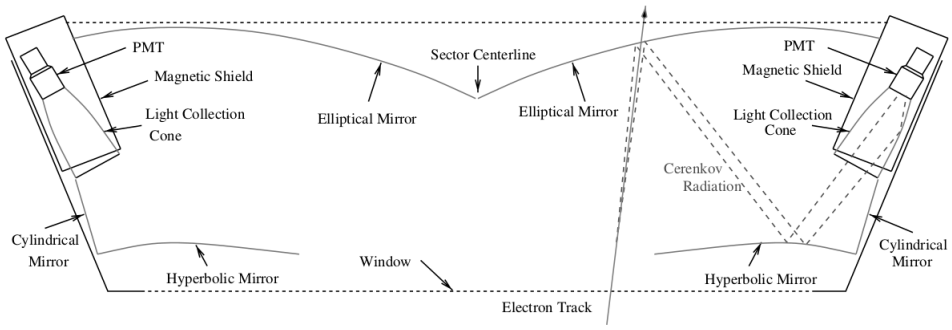

Figure 2.6: Schematic diagram of one Cherenkov segment, symmetric around the sector center. Shown an example of an electron trajectory with the collection of Cherenkov light to the PMT. The PMTs, magnetic shields, and light-collecting Winston cones lie in the region of the detector shadowed by the CLAS magnet coils, and thus do not affect the electron acceptance.

2.1.4 Time-of-Flight Counters (SC)

The time-of-flight counters are made of scintillator counters located radially outside the tracking system and Cherenkov counters but in front of calorimeters as can be seen in Fig. 2.2 and Fig. 2.3. They cover the polar angle θ between 8^o and 142^o, and the entire active range in ϕ. The thickness of the scintillator is 5.08 cm and is positioned perpendicular to the average local particle trajectory. At forward angles $\theta < 45^o$ the counters are 15 cm wide and 32-376 cm in length, for large-angle counters are 22 cm wide and 371-445 cm in length.

Details on the Time-of-flight system can be found in [25].

2.1.5 Forward Electromagnetic Calorimeters (EC)

The main functions of the electromagnetic calorimeter are the detection of electrons at energies above 0.5 GeV; photons with energies over 0.2 GeV; and detection of neutrons. It covers the θ angle up to 45^o. The calorimeters were made of alternating layers of scintillator strips and lead sheets with a total thickness of 16 radiation lengths. The ratio of lead-scintillator thickness was 0.24 leaving a total of 39 cm of scintillator and 8.4 cm of lead. For each EC module, the lead-scintillator layers are contained within a volume having a shape of a nearly equilateral triangle with projective geometry pointing to the nominal target position. Each EC module consisted of 39 layers, constructed with 10mm thick scintillator; followed by a 2.2mm lead sheet; and contained in a volume with a nearly equilateral triangle shape. For the readout system, 36 strips parallel to one side of the triangle with a rotation of 120^o in successive layers, giving rise to a set of views U, V and W, each one with 13 layer as seen in Fig. 2.7. Each of the views are further subdivided into an inner (5) and outer (8) stack, providing longitudinal sampling that helps to improve hadron/electron separation.

Details on the CLAS forward electromagnetic calorimeter system can be found in [26].

Performance studies include 10 cm fiducial cut from the edges of EC. The energy

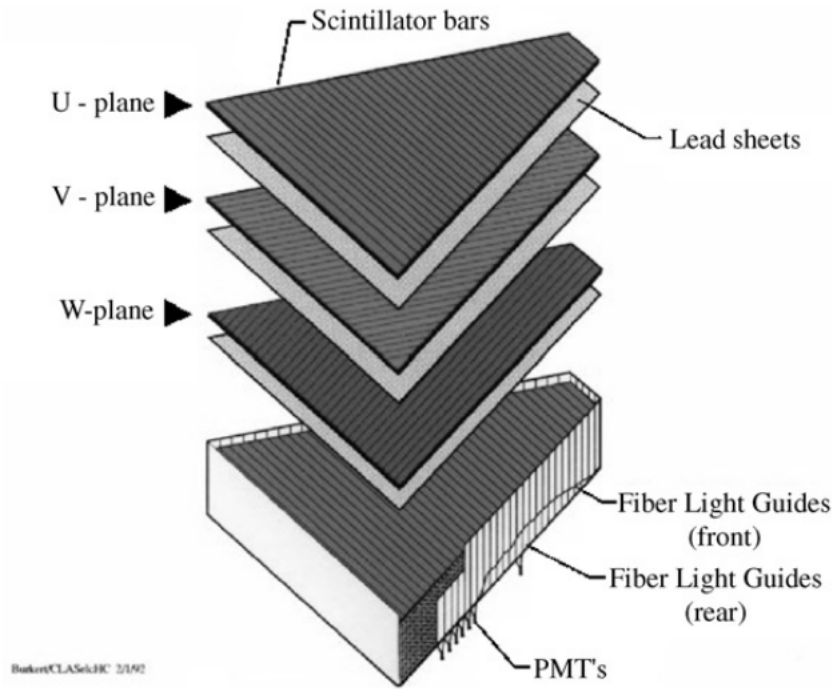

Figure 2.7: Exploded view of one of the six CLAS electromagnetic calorimeter modules.

resolution is:

$$\frac{\sigma}{E} = \frac{10.3\%}{\sqrt{E(GeV)}},$$

and has a negligible constant term.

The sampling fraction ranges from 0.25, for electrons around 0.5 GeV to 0.3 for electrons of 3 GeV and more. The position resolution is 2.3 cm for electrons above 0.5 GeV, and the timing resolution is around $\sim$ 200 ps.

2.2 Double-Target System

The design of the target was arranged for precision measurement of nuclear medium effects- such as the hadron attenuation and transverse momentum broadening- and the attenuation of rho mesons in nuclei to search for color transparency in a unpolarized

electron scattering electron beam of 4-5 GeV. To accomplish this goal, an effort was made to minimize the systematic uncertainties through a unique double-target design. This design is composed of two targets: one solid (Carbon, Aluminum, Tin, Iron or Lead), and one liquid (Deuterium). Both target are positioned a few centimeters apart exposed at the same time, and to the same electron beam.

The main reason to use a double-target system is related to time-dependent modulations of trigger efficiency, charged particle reconstruction efficiency, and acceptance corrections based on emergence and disappearance of inoperative channels. Other systematic uncertainties sources -such as atmospheric pressure variations and drift chamber gas composition variations- can be reduced by exposing two targets simultaneously to the electron beam.

The requirements for the target were as follows:

- Large acceptance for semi-inclusive and exclusive kinematics, plus a good match to the CLAS spectrometer acceptance.
- Minimal mass for low-energy particles at large angles ($70 - 140^o$ relative to the beam direction) as well as forward going particles.
- Approximately equal scattering rates for two targets in the beam simultaneously.
- One of the targets needed to be a stable deuterium cryotarget.
- Less than 2-3% of a radiation length of any target material to suppress secondary electromagnetic processes.
- Minimal entrance/exit window thicknesses for cryotarget to maximize target/window ratio.
- Rapid target changes for the heavy nuclear targets.
- Minimal mass in support structure.

A schematic of the cryotarget can be seen in Fig. 2.8. A full assembly of the double target is shown on Fig. 2.9. Each holder arm carries a different target and can be flipped on and off remotely to change the target on beam.

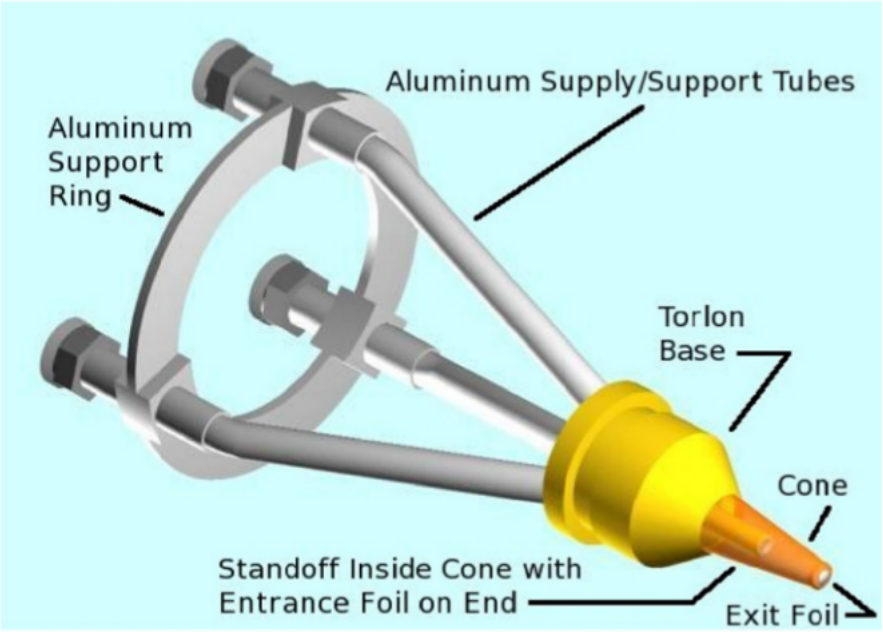

Figure 2.8: A schematic drawing of the cryotarget cell, wich shows the three support tubes through which cryogens flow; the entrance foil attached to the cylindrical stand-off; and the exit foil attached to the outer cone. The electron beam passes through the center of the support ring in the upper left part of the drawing, then through the entrance and exit foils in the lower right part of the drawing.

Details on the Target system can be found in [27].

In what follows, the solid targets used in the analysis are ^{12}C, ^{56}Fe ^{208}Pb.

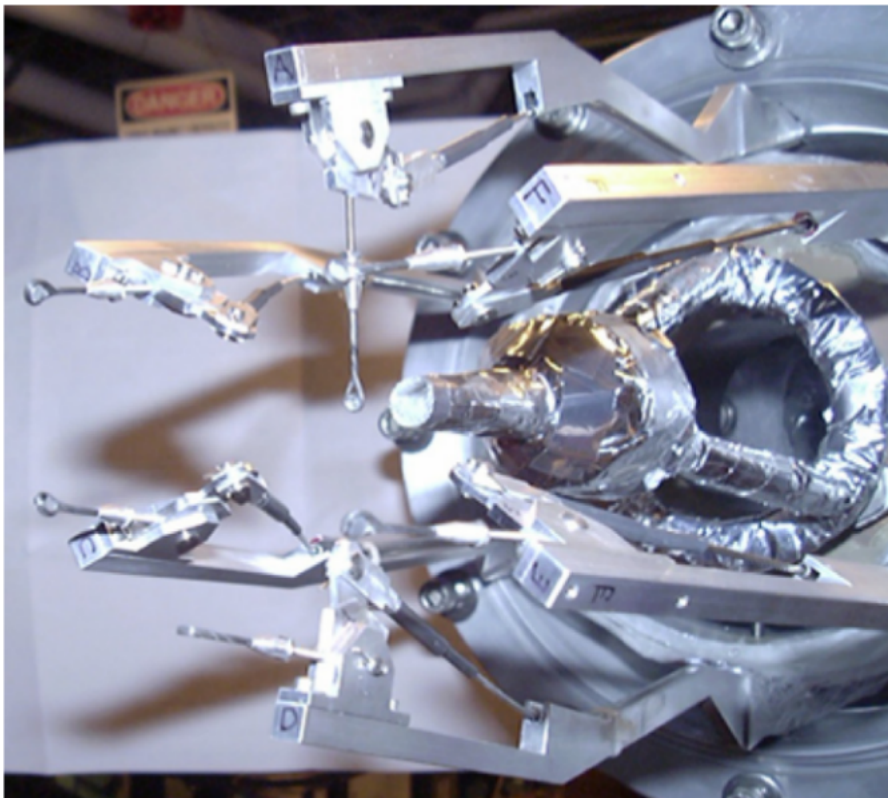

Figure 2.9: The full double-target assembly, which shows one solid target flipped on position; five solid targets retracted; and the thermally insulated cryotarget cell.

Chapter 3

Data Analysis

3.1 Analysis Tools

The raw data obtained from the experiment was stored in a BOS (Bank Object System) [28] format database in separated files for each run. The data is organized in banks, which are units of information corresponding to certain detector. The reconstruction procedure to convert raw data into particle information is named "cooking". The "cooking" is performed using USERANA software, which gives information of the reconstructed tracks in BOS format. The data is organized in terms of events, including the trigger electron followed by all the reconstructed particles detected after the trigger. The next step consists in taking the BOS format data from USERANA and convert them to ROOT [29] format files. This step is performed using the ClasTool software. ClasTool organizes the information in ClasTool-like structure using NTuple objects from ROOT. The links between different banks are included as pointers.

The last step is performed using Analyser [30], a c++ based class. Analyser takes the data from ClasTool and reduces it to NTuples with general information of the particles. This process is implemented in order to have a simpler format, as well as, easier and faster to work with.

Using the information stored, particles are identified and assigned an PID. In this study, electrons and π^+ were identified in order to measure Bose-Einstein pion correlations.

3.2 Electron Identification

The particles in the EVNT bank are ordered according to their arrival time to SC. Depending on the type of particle, some of them will leave tracks in all detectors and others in just a part of them. The information, regarding the sign of the electrical charge of the particles, is extracted from the DC looking at the curvature presented under the magnetic field produced by the torus magnet. If the particle bends inwards, it has a negative electric charge, on the contrary, if the particle is positive, it will bend outwards. To classify an event as a "good" one, the first particle identified in the event must be the scattered electron, hence the focus is on the first row of the EVNT bank. The basic requirements to identify a particle as an "electron" are listed below.

- The particle must leave a track in all detectors (DC, CC, SC, EC).
- The charge must be negative.

In terms of Bank information in the Analyser software, electron identification is required to be:

Requirement	Description
0 < EVNT.status < 100	Correct Status
rows in CCPB != 0	Must be information in the Cherenkov Counter bank
rows in ECPB != 0	Must be information in the Electromagnetic calorimeter particle bank
rows in SCPB != 0	Must be information in the Scintillator counter particle bank
EVNT.CCStat > 0	Valid pointer to CCPB bank
EVNT.SCStat > 0	Valid pointer to SCPB bank
EVNT.DCStat > 0	Valid pointer to DCPB bank
EVNT.ECStat > 0	Valid pointer to ECPB bank
EVNT.Charge == -1	Particle must have negative charge

Table 3.1: Bank information in the Analyser software required for electron identification.

If these requirements are fulfilled, the next step is to make π^-/e^- separation by using the information on CCPB. We can differentiate e^- from π^- measuring the electromagnetic radiation emitted by them passing through a medium, called Cherenkov radiation. Cherenkov radiation is a type of electromagnetic radiation emitted by a

charged particle passing through a medium with a velocity larger than the velocity of light in such medium, and the number of photons emitted by the charged particle increases with its velocity. A minimum momentum threshold for each type of particle is required to emit Cherenkov radiation, depending on the mass of the particle. In this case, charged pions need a minimum momentum of 2.5 GeV to emit Cherenkov light, compared to electrons that need just few MeV. From the distribution of the number of photons collected by the PMTs of the CC, a clear peak with low number of photo-electrons is observed. This peak correspond to the π^- signal. A minimum number of 2.5 photo-electrons is required in each sector of the CC in order to select the particle as an electron. A cut in the number of photoelectrons can be seen in Fig. 3.1.

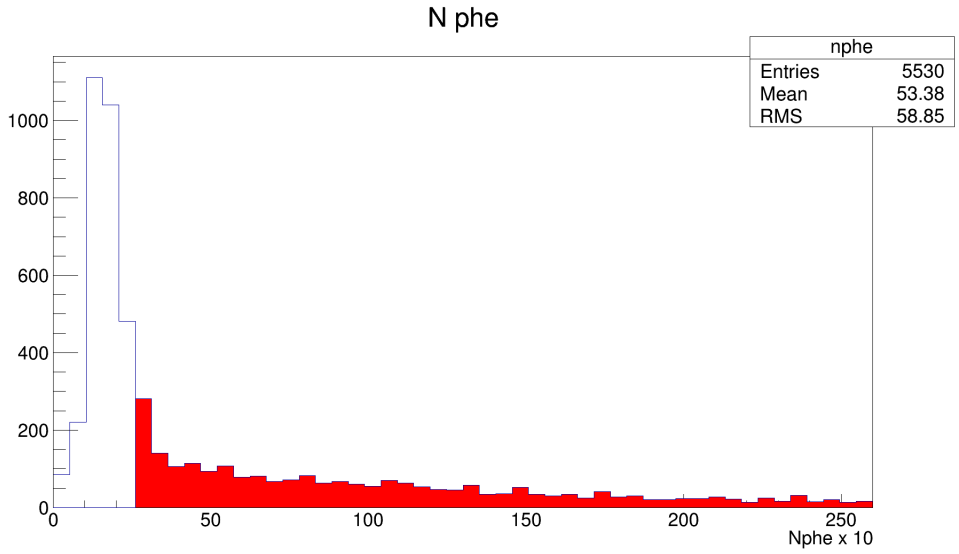

Figure 3.1: Number of photo-electrons threshold on CC. The peak on the left side come from π^- contribution. The red filled area corresponds to the electron selection.

Even with the electrons identified, some additional cuts are necessary in order to assure the quality of the data. As a result of the detector being divided in six sectors, there is a gap between the sectors with poor acceptance because when a particle hit the edge of the detector, the electromagnetic shower is not fully contained within the detector. In order to reduce systematic uncertainties due to acceptance, a fiducial volume is selected where the acceptance is large and uniform. A set of cuts called "fiducial cuts",

developed by Lorenzo Zana, removed the data near the edges of the detector where the acceptance decreases. The difference between electrons selected with and without fiducial cuts applied can be seen in see Fig. 3.2.

After the electrons are identified, the next step is to select events with kinematics in the DIS regime. According to the wave length of the virtual photon: $\lambda \approx 1/Q$, the selection of $Q^2 > 1.0$ allows to resolve partons inside the nucleons. To exclude the hadrons coming from nuclear resonance decay (e.g. Δ^{++}) a cut on the invariant mass of the electron-nucleon interaction W is applied: $W > 2.0$. Besides that, one of the possible sources of the data contamination are the radiative effects which are becoming more important for larger values of the DIS variable y, hence a cut $y < 0.85$. Fig 3.3 show electrons with all selection cuts applied.

3.2.1 Vertex Cuts

After a particle is identified as electron, the next step is to identify if it interacted with the solid or liquid target. To achieve this, a vertex cut is applied on the Z variable that represents the position of the vertex along the beam axis. The vertex cuts on Z for each sector are presented in the Table 3.2, Figure 3.4 shows the Z distribution of the vertex position of electrons, and Figure 3.5 shows vertex cuts for each sector.

Sector	Liquid Target	Solid Target
0	-32.50 ; -28.00	-26.50 ; -20.00
1	-32.50 ; -27.50	-26.00 ; -20.00
2	-32.00 ; -27.25	-26.65 ; -20.00
3	-32.00 ; -27.75	-25.85 ; -20.00
4	-32.50 ; -28.35	-26.65 ; -20.00
5	-33.50 ; -28.75	-27.15 ; -20.00

Table 3.2: Vertex cuts on Z to identify electron target interaction.

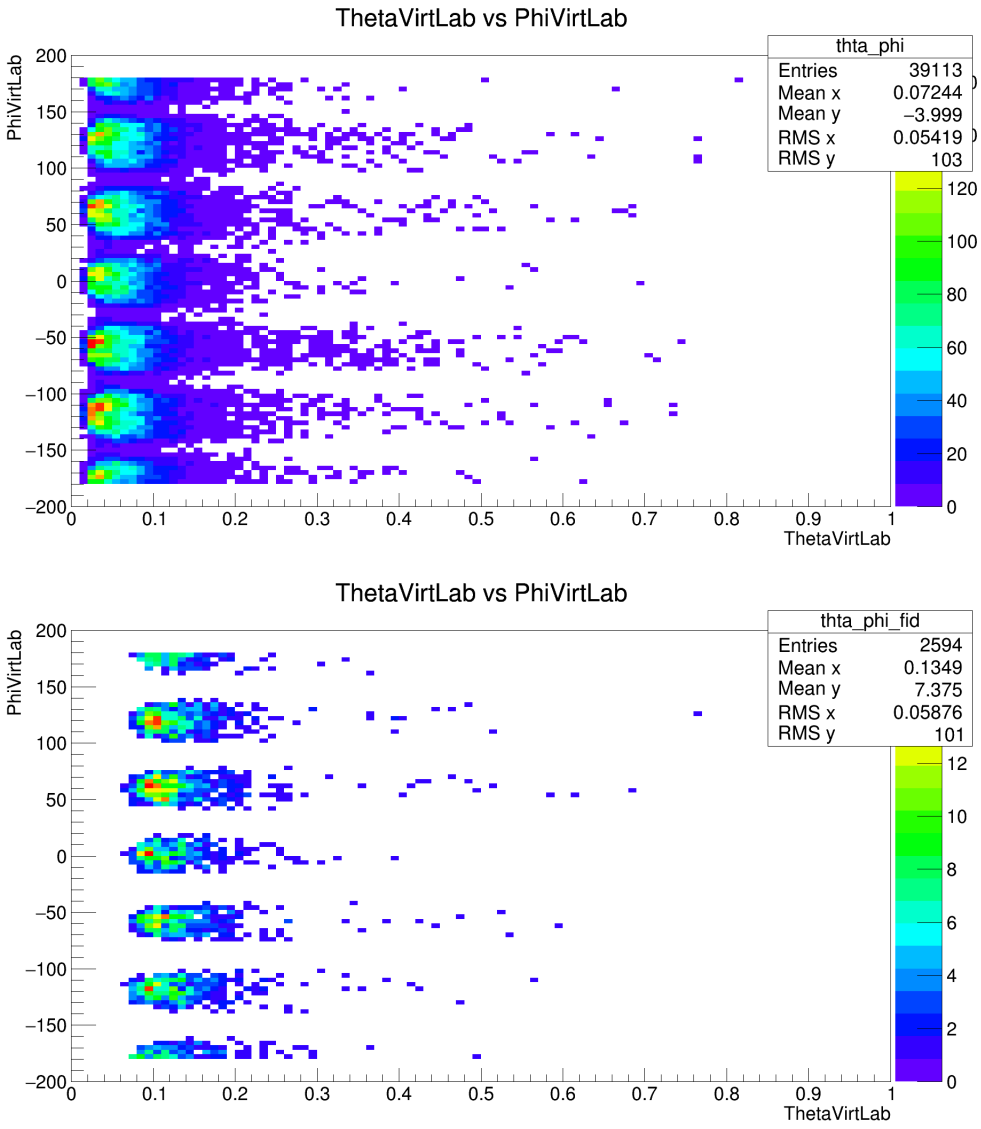

Figure 3.2: θ_{lab} vs ϕ_{lab} for electron candidates in each of the six sectors. The upper plot shows electron candidates before fiducial cuts ; the lower plot shows the electrons after fiducial cuts, the hits at the edges of each sector are removed.

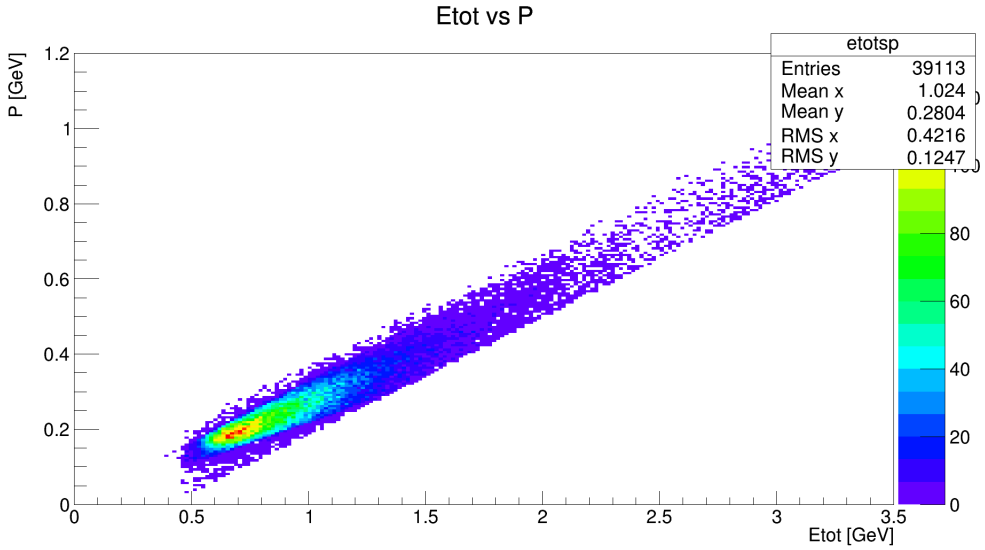

Figure 3.3: Electron phase space after all cuts applied.

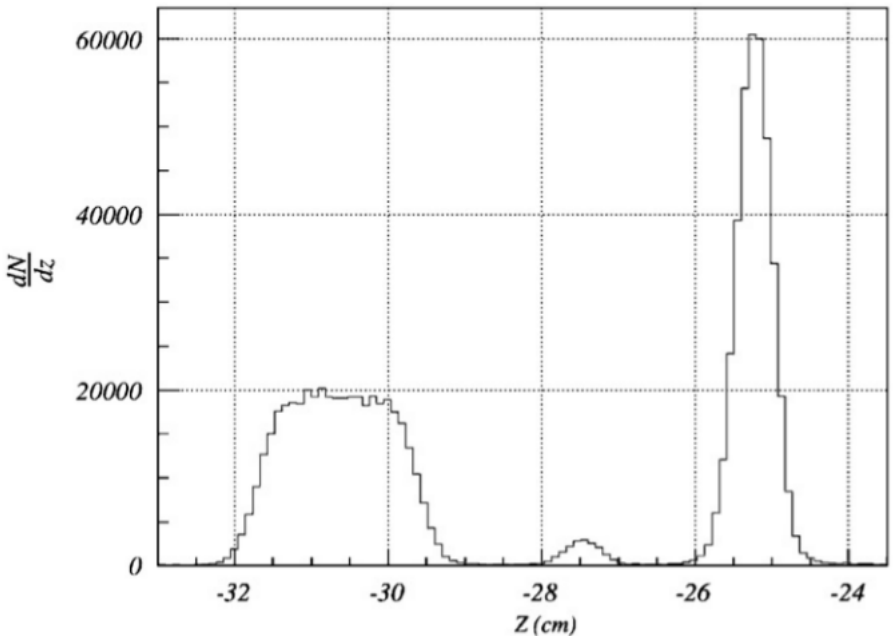

Figure 3.4: The rightmost peak corresponds to the solid target and the leftmost distributions corresponds to the liquid deuterium target. The smallest center peak shows the aluminum foil between both targets.

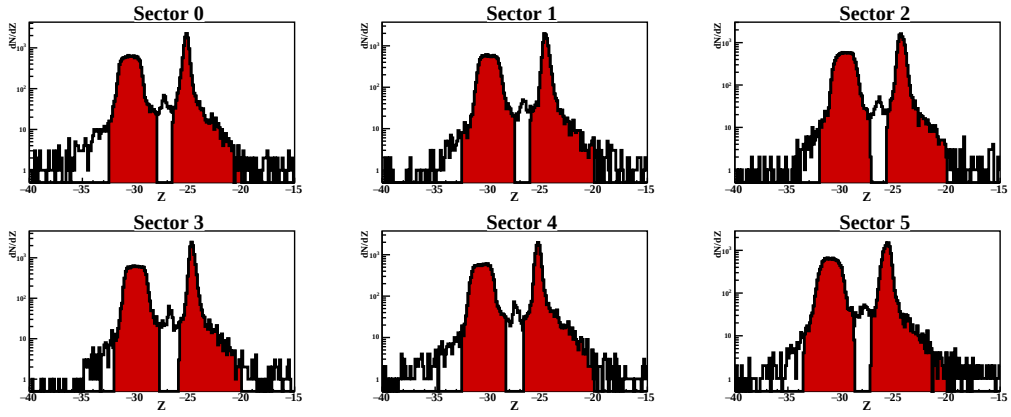

Figure 3.5: Vertex for the target discrimination. Events coming from liquid and solid target are shown in red in the left and right side respectively. Plots made by Sebastián Morán

3.3 π^+ Identification

The main particles on this analysis were positive pions π^+. The principal task on the selection process was to discriminate them from other positive hadrons. Positive pions were identified using positive reconstructed tracks with track signals in the SC, DC.

In terms of Bank information in the Analyser software, it is expressed as:

- 0 < EVNT.status < 100
  rows in SCPB != 0
  EVNT.SCStat > 0
  EVNT.DCStat > 0

- EVNT.Charge == 1

To separate positive pions from kaon and proton contamination, we used a "time-of-flight" discrimination technique. The selection was made using information from the tracking system and the time-of-flight system to determine the timing difference between a positive hit and the outgoing electron. This time difference is called TimeCorr4

(Δt) and has the following form:

$$\Delta t = \frac{L^{e^-}_{flight}}{c} - t^{e^-}_{flight} + t_{flight} - T_{RFI} - \frac{L_{flight}}{\sqrt{(\frac{M_{\pi^+}}{p})^2 + 1}} \tag{3.1}$$

where $t^{e^-}_{flight}$ and t_{flight} are correspondingly the electron's and charged particle's time of flight from the interaction vertex to the scintillator plan. $L^{e^-}_{flight}$ and L_{flight} are the pathlenghts from the vertex to the TOF counters. M_{π^+} is the π^+ mass and p is the momentum of the charged particle. The T_{RFI} is an additional timing correction using the radio frequency signal sent from the accelerator injector.

The idea with this technique is to compare the theoretical time for a π^+ with a given momentum with the measured time taken for the particle to reach the SC detector. Particles heavier than the searched particle would take more time to reach the SC than the theoretically expected time. In a similar way, lighter particles would take less time. Cuts around 0 [ns] in time difference between the theoretical and measured time TimeCorr4 are applied for different momentum bins to select the π^+. These cuts are summarized in Table 3.3.

Momentum bin [GeV/c]	TimeCorr4 [ns]
0.00 ; 0.25	-0.70 ; 0.70
0.25 ; 0.50	-0.70 ; 0.65
0.50 ; 0.75	-0.70 ; 0.65
0.75 ; 1.00	-0.70 ; 0.65
1.00 ; 1.25	-0.55 ; 0.55
1.25 ; 1.50	-0.50 ; 0.55
1.50 ; 1.75	-0.50 ; 0.40
1.75 ; 2.00	-0.48 ; 0.40
2.00 ; 2.25	-0.50 ; 0.40
2.25 ; 2.50	-0.50 ; 0.40
2.50 ; 2.70	-0.50 ; 0.40

Table 3.3: TimeCorr4 cuts for π^+ for different momentum bins.

Plots in Fig. 3.6 show the TimeCorr4 and mass distribution for positive particles

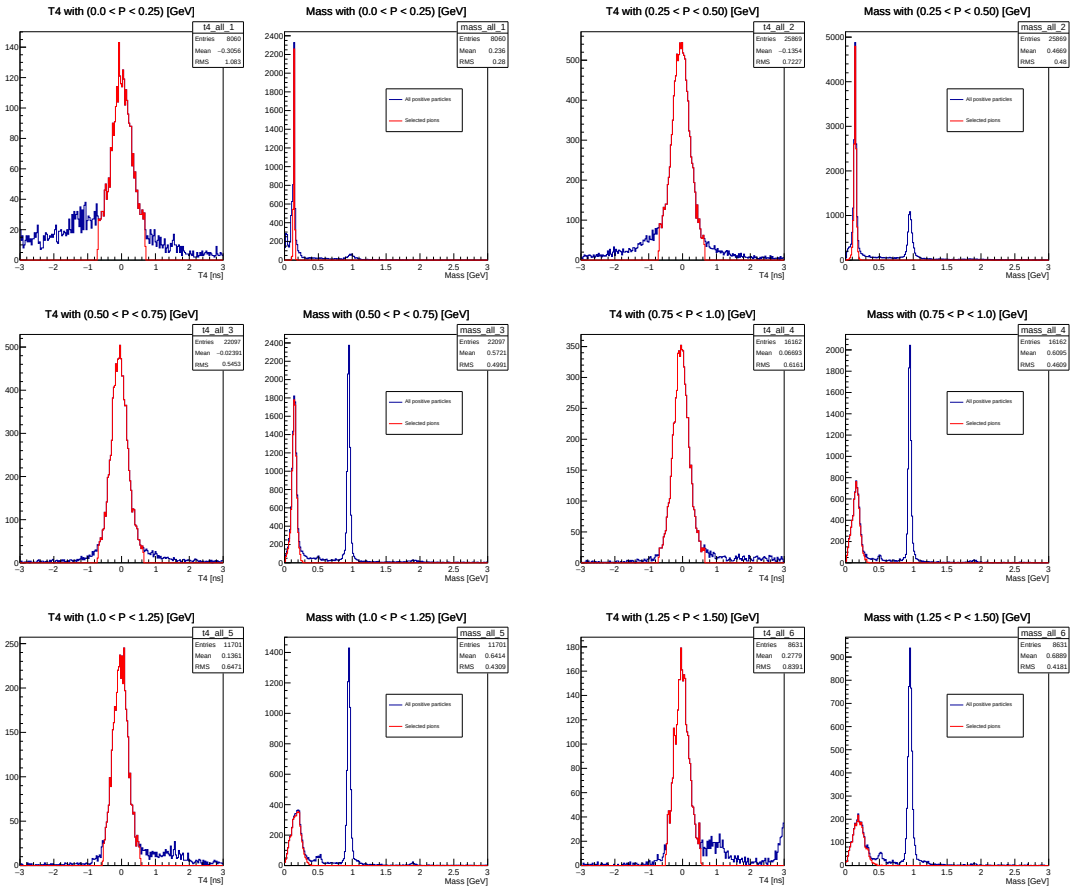
T4 with (0.0 < P < 0.25) [GeV]
t4_all_1
Entries 8060
Mean −0.3056
RMS 1.083
T4 [ns]
Mass with (0.0 < P < 0.25) [GeV]
mass_all_1
Entries 8060
Mean 0.236
RMS 0.28
All positive particles
Selected pions
Mass [GeV]
T4 with (0.25 < P < 0.50) [GeV]
t4_all_2
Entries 25869
Mean −0.1354
RMS 0.7227
T4 [ns]
Mass with (0.25 < P < 0.50) [GeV]
mass_all_2
Entries 25869
Mean 0.4869
RMS 0.48
All positive particles
Selected pions
Mass [GeV]
T4 with (0.50 < P < 0.75) [GeV]
t4_all_3
Entries 22097
Mean −0.02381
RMS 0.5453
T4 [ns]
Mass with (0.50 < P < 0.75) [GeV]
mass_all_3
Entries 22097
Mean 0.5721
RMS 0.4991
All positive particles
Selected pions
Mass [GeV]
T4 with (0.75 < P < 1.0) [GeV]
t4_all_4
Entries 16162
Mean 0.06693
RMS 0.6161
T4 [ns]
Mass with (0.75 < P < 1.0) [GeV]
mass_all_4
Entries 16162
Mean 0.6095
RMS 0.4609
All positive particles
Selected pions
Mass [GeV]
T4 with (1.0 < P < 1.25) [GeV]
t4_all_5
Entries 11701
Mean 0.1361
RMS 0.6471
T4 [ns]
Mass with (1.0 < P < 1.25) [GeV]
mass_all_5
Entries 11701
Mean 0.6414
RMS 0.4309
All positive particles
Selected pions
Mass [GeV]
T4 with (1.25 < P < 1.50) [GeV]
t4_all_6
Entries 8631
Mean 0.2779
RMS 0.8391
T4 [ns]
Mass with (1.25 < P < 1.50) [GeV]
mass_all_6
Entries 8631
Mean 0.6889
RMS 0.4181
All positive particles
Selected pions
Mass [GeV]

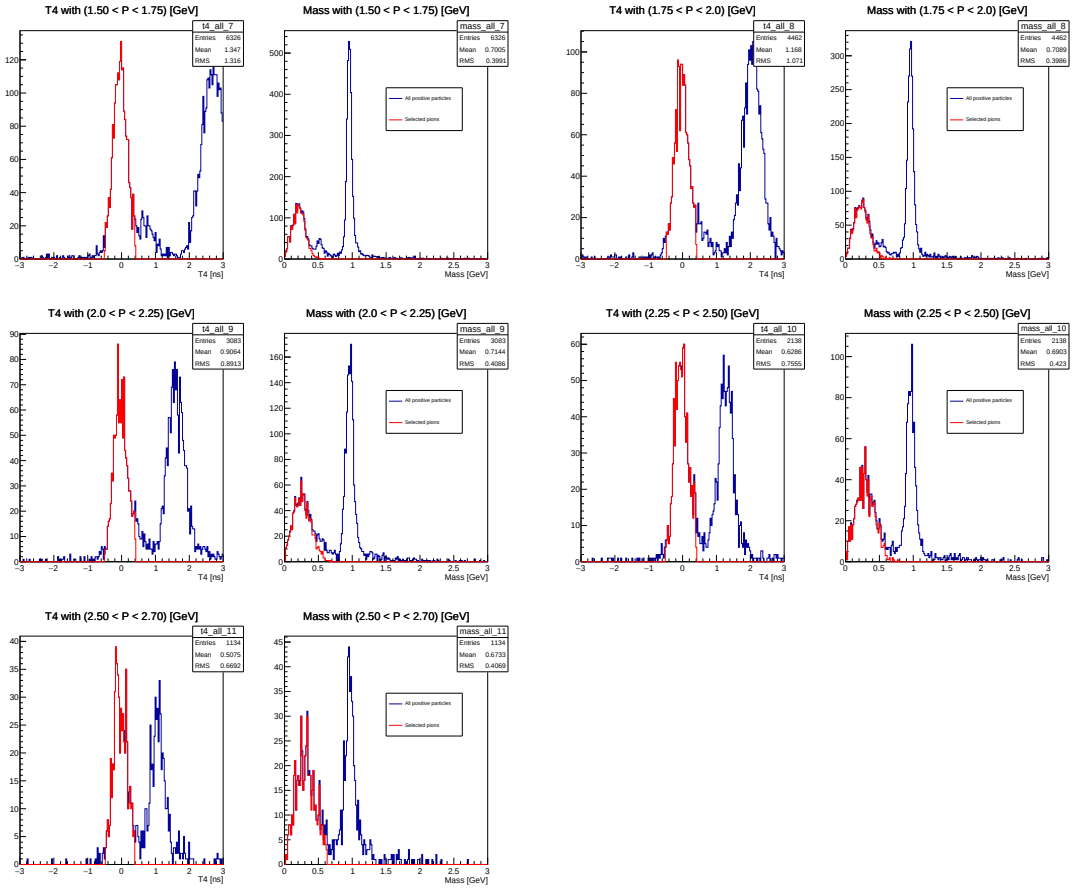

Figure 3.6: TimeCorr4 cuts. π^+ selected in red from all positive candidates that satisfied all cuts prior to time of flight cuts. T4 and mass distributions are presented on the left and right side respectively.

that fulfilled selection cuts mentioned in each momentum bin. All positive hadrons are plotted in blue and the selected pions that satisfy TimeCorr4 cuts are shown in red. A clear peak can be seen at the proton mass.

For pions with energies higher than 2.7 GeV, CC is used. Over this energy threshold, pions start to emit Cherenkov Radiation, a kind of electromagnetic radiation emitted when a charged particle moves faster than light in the medium. Heavier hadrons will not emit Cherenkov radiation at this energies. We request particles with more than 2.5 photo electrons emitted. In the final analysis it was decided to not include pions in this momentum range because hadron discrimination starts to get worse and proton and contamination is expected to be higher.

For π^+, we also apply fiducial cuts in a similar way we applied to electrons as mentioned in 3.2 to ensure good quality data. We made a cut in θ_{lab} and ϕ_{lab} variables to remove hits close to edges of the detector where acceptance is worse, and reconstruction is less reliable.

Identified π^+ are shown in Fig. 3.7. The red dots show pions selected. Proton, kaon and even deuterium signals can also be seen.

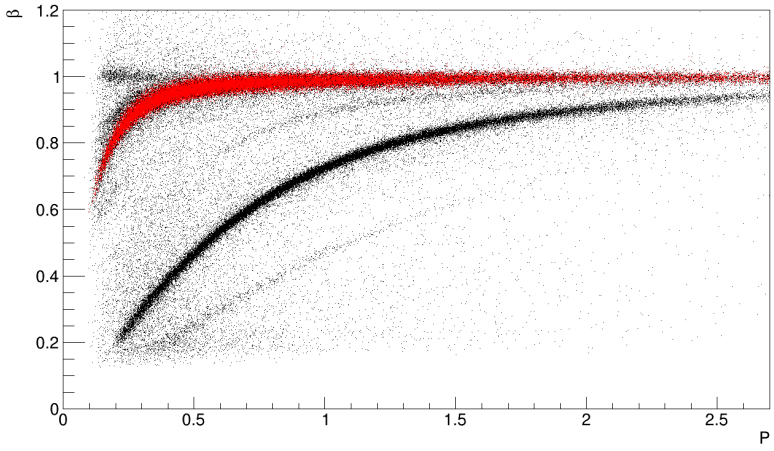

Figure 3.7: π^+ selected shown in red after applying all selection cuts. Particles taht not passed the selection cuts are shown in black. Protons, kaons and positrons can be seen

3.3.1 Pion pair Construction

In order to construct the correlation function, we need the two-particle probability distribution directed by Bose-Einstein symmetrization as well as the single particle distributions described in Eq. 1.1. The single particle distributions for the denominator of this ratio are difficult to measure experimentally, so instead of using two single particle distribution, a common practice is to replace both single-particle distribution by a reference two-particle probability density distribution, also called background distribution $D_b(p_1, p_2)$. The background distribution is constructed experimentally creating uncorrelated pion pairs that ideally behaves exactly as $D(p_1)D(p_2)$ with the exception of not containing Bose-Einstein correlations. Therefore the experimentally constructed Bose-Einstein correlation becomes:

$$R_{(p_1,p_2)} = \frac{D(p_1, p_2)}{D_b(p_1, p_2)} \tag{3.2}$$

The numerator from the experimental Bose-Einstein correlation is constructed from the number of π^+ same-event pairs that satisfy the imposed cuts. This distribution, also called signal distribution, contains identical pion-pairs coming from the same source and, therefore, correlated by Bose-Einstein statistics.

The number of $\pi^+\pi^+$ same-event pairs for all different targets studied are presented in the following table:

Target	Number π^+ in 2+ pion events	Number of same-event pairs
D2	4.465.779	2.279.010
C	995.063	517.690
Fe	1.628.385	850.902
Pb	454.873	236.911

Table 3.4: Number of positive pions slected from multiple π^+ events and same-event pairs constructed from them, for different nuclear targets.

For good determination of the Bose-Einstein effect, is highly important to have a correct background distribution, the denominator in Eq. 3.2. The background can be constructed in different ways that satisfies the absence of Bose-Einstein effects but

maintain other properties found in the same-event distribution. The methods most widely used in literature are the following:

- Method of unlike-sign pairs.
- Method of event mixing.

In the method of unlike-sign pairs, the background distribution is constructed in the same way as the signal distribution with the exception of pairing two pions of the opposite charge ($\pi^+\pi^-$), instead of two identical pions with the same charge $\pi^+\pi^+$. In this case, as the two particle are not identical, their wave functions do not interfere leading to the Bose-Einstein effect. One of the disadvantages of these methods is the possible contamination of unlike-sign pion pairs coming from resonances. Another disadvantage is that the detector efficiency and contamination in the selection method of positive and negative pions are not identical.

In the method of event mixing, the background distribution in constructed using $\pi^+\pi^+$ but the two particles, needed to construct the pair, are taken from different events. In our case, we tried different ways to do the mixing of events, that is discussed later in the systematic errors section. With this method for the construction of the background, Bose-Einstein correlations from the original events are lost because both pions were originated from different events and, therefore, have different sources. The main problem related to the mixing method is the violation of energy-momentum conservation when selecting pions from two different events. Some of the pion-pairs in the background distribution are created outside the phase space of the same event pion-pair distribution that leads to higher number of pairs with high Q_{12} compared to the same event part.

In this work, the method of event mixing was chosen for the construction of the background distribution for the calculation of the Bose-Einstein correlation function. The main reason for this decision was that we have a better identification of π^+ compared with π^-, which leads to more consistent results and a better correlation function shape. In the mixing method, the pions are selected from different events. In consequence, this procedure will pick events with virtual photons with different orientations in the lab frame. Then to conserve the collinearity between the virtual photons from

both events, for each pair we rotated the second event selected to align both virtual photons as shown in Figure 3.8. In this sketch, two events with their respective virtual photon and scattered electron are shown in different colors. The second event is rotated into the first one by the angle $\Delta\varphi$, which is defined as the difference between both virtual photons. It is important to emphasize that not only the virtual photon is rotated but also the complete event, including the selected pion. The number of $\pi^+\pi^+$ pairs constructed using the method of event mixing is arbitrary; we can virtually form as many pairs as we want. In order to get good statistics, we created 3 times the number of pairs from the signal distribution.

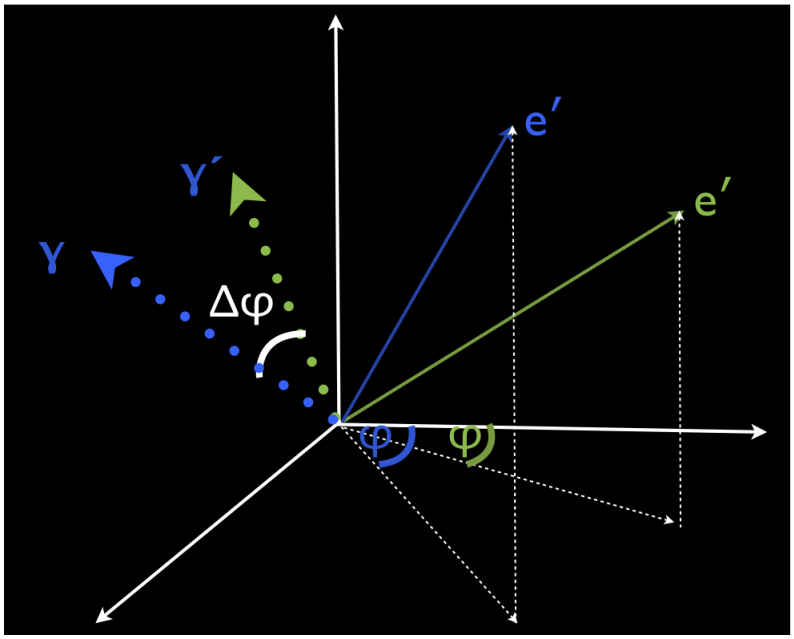

Figure 3.8: Sketch of the rotation used to preserve the collinearity of photons of both events in the mixing method. Different events are shown in different colors. The second event is rotated into the first one by the angle $\Delta\varphi$ in order to align both virtual photons.

Only π^+ with measured momentum $P < 2.7$ GeV were included in the construction of the pairs. The reason behind this is that pion identification up to these energies is based on the information obtained mainly from the SC and DC, which is more reliable and is expected better purity of the pion sample, for momentum $P > 2.7$, proton contamination is expected to be higher.

Pion pairs, from both the same event distribution and background distribution, are created taking events with at least two particles identified as π^+. All events with only one identified positive pion are discarded. For events with three or more π^+ identified, all possible pair combinations are included, i.e., for a three positive pion event, we can construct 3 different pion pairs; for a four pion event, we get 6 pion pairs, etc. Special emphasis has to be taken to not make double counting. Most of the selected pairs comes from only two-pion events (97.3%), and a little percentage comes from events with three (2.7%) or more (<0.1%) identified pions.

With both, the signal and background distributions constructed shown in Fig.3.9, we calculated the correlation functions shown in Fig. 3.10 using Eq. 3.2 for different nuclear targets.

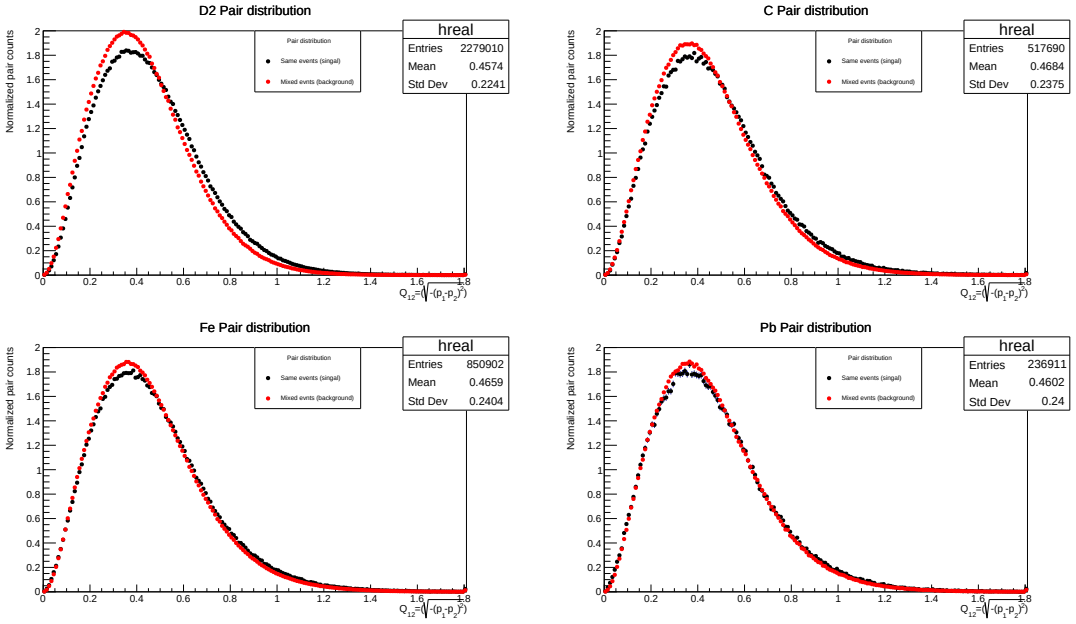

Figure 3.9: π^+ pairs normalized distributions from data for all nuclear targets in the Q_{12} variable. Black curves correspond to same event pairs (signal distribution) and red curves correspond to mixed rotated events pairs (background distribution).

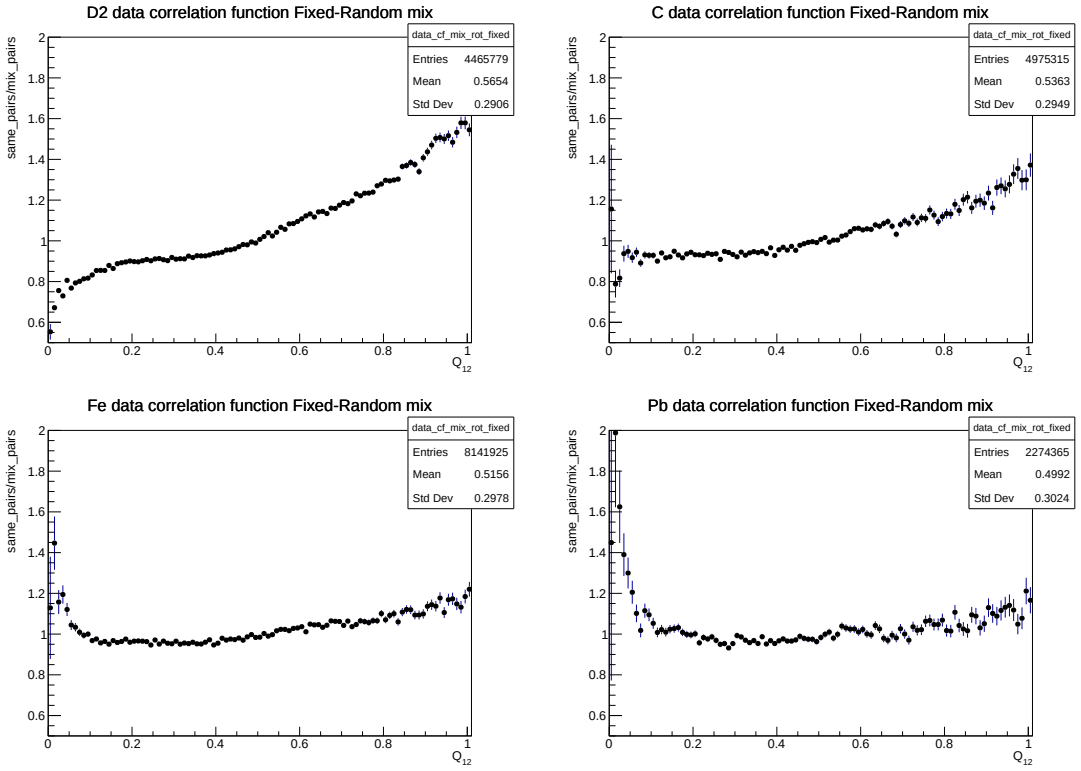

Figure 3.10: Correlation function obtained by dividing the signal distribution by the background distribution for different nuclear targets. Top left Deuterium, top right Carbon, bottom left Iron, bottom right Lead.

3.3.2 Simulations

Simulations are an important part in the understanding of experiment based problems and are critically essential in the data's correction. The simulations used for both, the double ratio correction and the close track efficiency calculation, discussed in sections 3.3.4 and 3.3.3, were performed by Hayk Hakobyan and are explained in detail in [31]. The simulated events consist in two sets, the generated events and the reconstructed events. By reconstructed events, it is meant the generated events after passing through the Monte-Carlo $\rightarrow$ GSIM $\rightarrow$ GPP $\rightarrow$ USERANA sequence, explained as follows.

Pythia 6.319 was the Monte-Carlo event generator used. In order to feed the events to GSIM, the output file of the Monte-Carlo simulation was converted into BOS database format containing the "PART" banks, which containing the information from the event generator. The GSIM program creates an idealized model of the CLAS spectrometer. The GSIM program is built on the base GEANT 3 simulation package and allows to model the response of the spectrometer to the passage of particles through it including, such processes as energy loss and radiation of secondary particles during transports through different parts of CLAS.

In order to eliminate signals from dead channels, the GSIM Post Processor (GPP) program was used to remove signals from dead wires in the drift chambers and bad tubes in the scintillator counters.

The GSIM files were processed with the USERANA program to reconstruct the simulated events. The executable of the reconstruction program was built with the same libraries which were used for the processing of the actual data from the EG2 running period. In the final stage, the same cuts used on the experimental data were used to the simulated output data.

As an important note, these simulation did not include Bose-Einstein correlations at generator level, which let us to apply a correlation function calculated from reconstructed events as a correction to the data.

The simulated events were then processed in the exact same chain as the data in order to construct the simulated correlation function for each of the four nuclear targets as is shown in Fig. 3.12. The pion pair distributions needed to construct the simulated

correlation function are shown in Fig. 3.11.

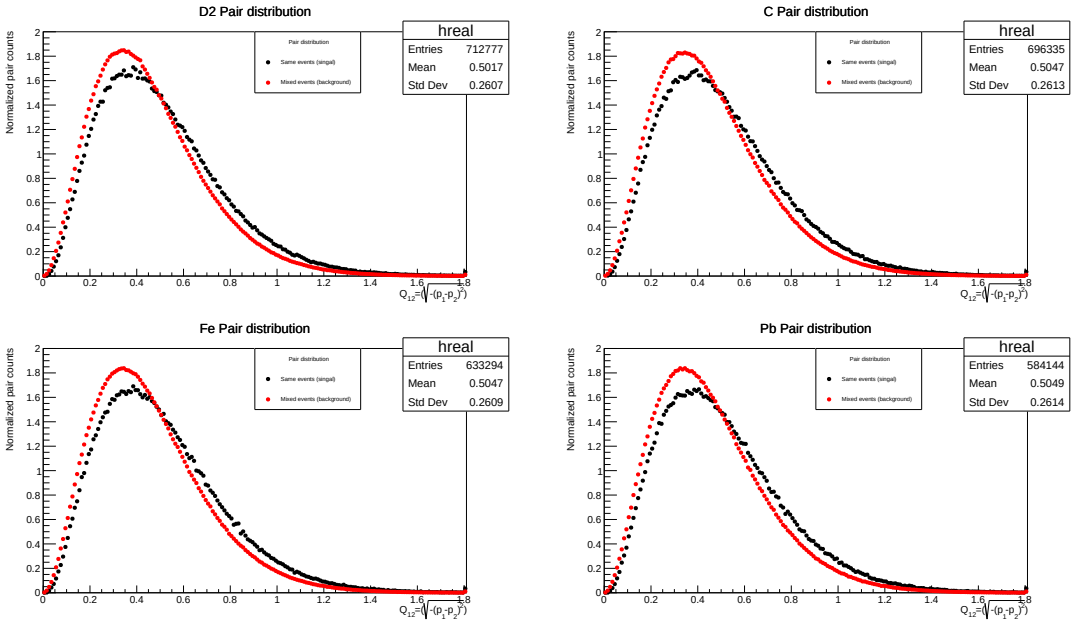

Figure 3.11: π^+ pairs normalized distributions from simulations for all nuclear targets in the Q_{12} variable. Black curves correspond to same event pairs (signal distribution) and red curves correspond to mixed rotated events pairs (background distribution).

We can see in 3.12 a completely different shape for all four nuclear targets at small values of Q_{12} mainly because of two reasons. The first one corresponds to the lack of enhancement in the signal distribution because the Bose-Einstein effect is not present. The second one is related to the efficiency of the detector to detect very close tracks (small Q_{12}), which is discussed in detail in the next section and valid for both data and simulation.

3.3.3 Close-Track Efficiency

Two particles with same charge and close momenta are a difficult configuration to measure. This happens when two particles in an event travel close to each other through the detector with very close trajectories, so they could hit the same or neighboring detector cells and their tracks can be misdetected as one particle instead of two separated tracks

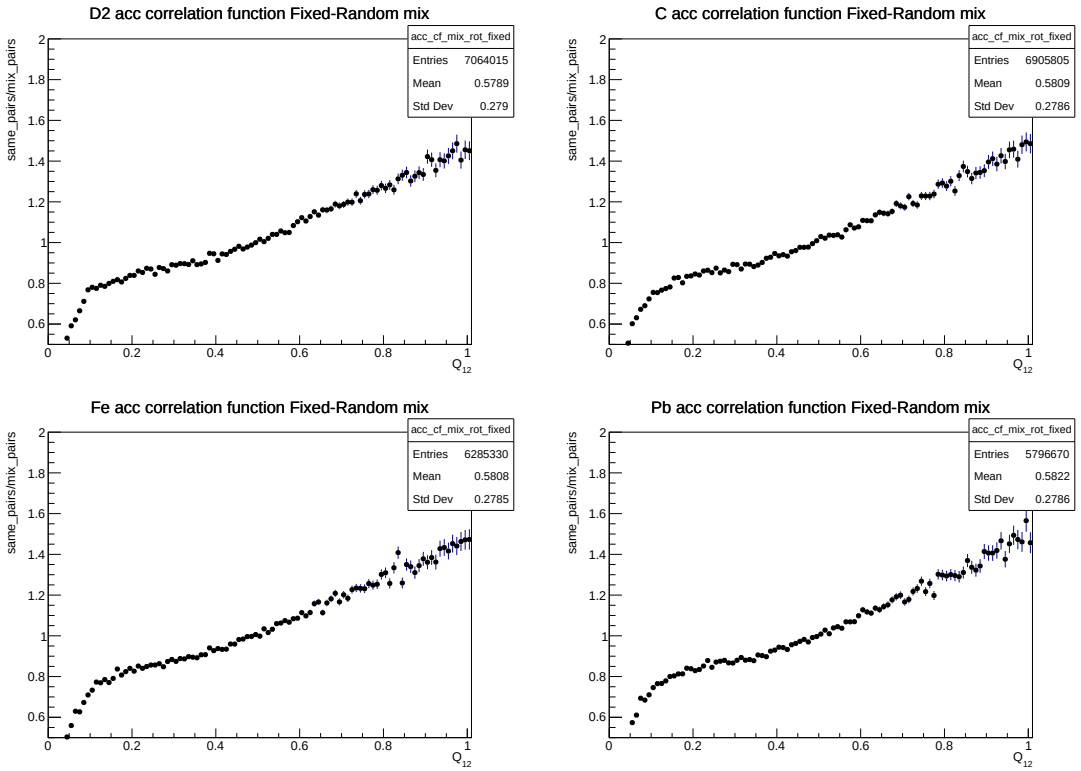

Figure 3.12: Correlation function obtained from reconstructed simulated events for different nuclear targets. A clear drop at low Q^2 can be seen, this behaviour is related to the absence of Bose-Einstein correlations in the simulations combined with low acceptance for close particle tracks.

as shown in Fig. 3.13. In consequence there is a possibility of losing one track, and thus, a pair. Thus, the probability to loss one of the two tracks will be higher if the tracks are closer to each other.

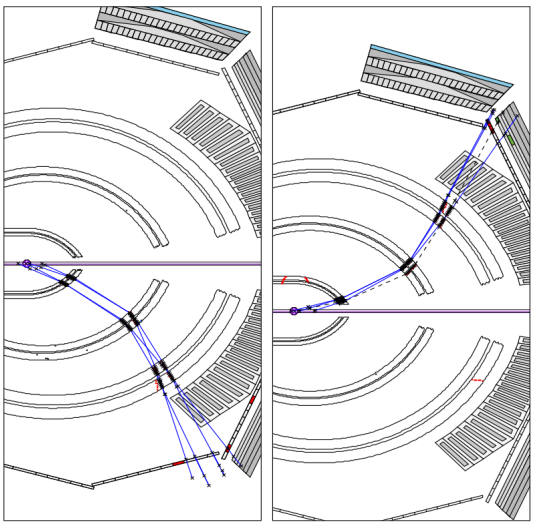

Figure 3.13: Example of two proton close tracks. Two tracks very close with each other can be detected as a single track.

Close-track momenta efficiency in CLAS detector was studied by K.Mikhailov, A. Stavinsky, and A. Vlassov in [32]. In this study, three different methods were used to measure this effect. The first method is the most conventional and is based on Monte-Carlo simulations. The second method used experimental pairs made of two particles with different masses. The third method uses well identified protons and consists in the merging of different events at detector hit level to create new artificial events which were reconstructed later.

The close track efficiency $\varepsilon(q)$ is defined as:

$$\frac{d\sigma_{measured}}{d\nu dQ^2 d\vec{p_1} d\vec{p_2}} = \varepsilon(q)\varepsilon_1(\vec{p_1})\varepsilon_2(\vec{p_2})\frac{d\sigma}{d\nu dQ^2 d\vec{p_1} d\vec{p_2}} \tag{3.3}$$

where ε_1 is the single particle reconstruction efficiency. $\varepsilon(q)$ is extracted studying the ratio:

$$\frac{R_{measured}(q)}{R(q)generated} = \varepsilon \tag{3.4}$$

In this analysis two of the three previous methods were tested with some differences.

In the first method based on Monte-Carlo simulations, generated and reconstructed events were analyzed, and events with the following pairs combinations were selected: pp, $p\pi$ and $\pi\pi$. Then, the correlation function were calculated for each pair type separately using 3.4, where $R(q)$ correspond to the correlation function using generated events and $R_{measured}$ was the correlation function with reconstructed events. We took -for the close track efficiency analysis- protons in the range $0.3 - 1.0$ GeV and pions with momentum range of $0.15 - 0.6$ GeV.

The second method, based in experimental data, is associated with the fact that particles with the same charge and close momenta in the laboratory reference system, but different masses leave the same track in the detector compared to identical particles. Thus, close track efficiency is expected to be the same. There should be no sharp singularities for small momenta difference $\overrightarrow{q}$ in the correlation function of pairs with different masses in the laboratory system. With this method, the detection efficiency for a pair of identical particles with small relative momenta are determined by measuring the correlation function of particles with different masses and small relative momenta. The dependence of such correlation function could be interpreted as the efficiency on $\overrightarrow{q}$.

A comparison between efficiency curves for both methods is shown in Fig.3.14. We can see a clear drop on the efficiency on pairs detection at low momentum difference between particles of the pairs, and a clear consistency between both methods and type of pairs.

The close-track efficiency results were not applied directly on the construction of the Bose-Einstein correlation function. However, is a good indication that most pairs at low 4-momenta difference are lost, reduces the strength of the correlation, thus data had to be corrected in some way, which was achieved by the double ratio correction shown in section 3.3.4.

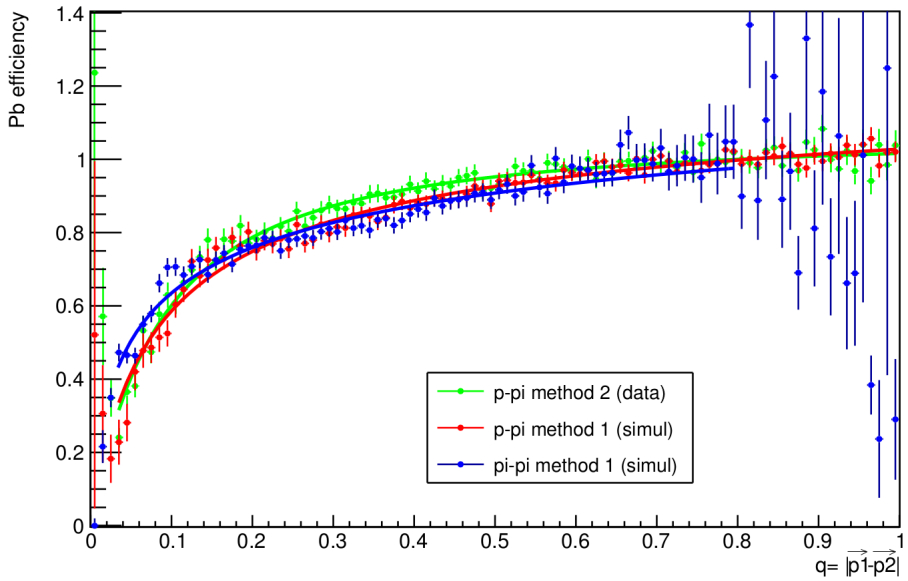

Figure 3.14: Close track efficiency measured with different methods. A clear drop in efficiency can be seen at low q.

3.3.4 Double Ratio Correction

We discussed in section 3.3.1 that the correlation function calculated from data has some undesirable behaviour at high Q_{12}. Such behaviour is related to the phase space of the $\pi^+\pi^+$ pairs constructed with method of event mixing for the background distribution. We also showed that the experimental efficiency for close-tracks get worse at low momentum difference Q_{12} of the pairs. We must add that our correlation function is subject to long-range correlations that affect the final Bose-Einstein correlation shape.

The double ratio correction is an important part in the Bose-Einstein analysis. This helps to correct experimental systematic biases found in the correlation function obtained in data (Fig. 3.10) related to the experiment and our analysis methods.

The double ratio technique consists on dividing the experimental correlation function obtained from data by a correlation function constructed in the exact same way as the experimental one, but using reconstructed Monte-Carlo events. The simulation

used for the correction should include the same behaviour than data but must not include Bose-Einstein correlations.

Double ratio for the correlation function is defined:

$$R(Q_{12}) = R(Q_{12})^{data}/R(Q_{12})^{simul} \tag{3.5}$$

$$R(Q_{12}) = (\frac{D(Q_{12})}{D(Q_{12})}_{mix})^{data}/(\frac{D(Q_{12})}{D(Q_{12})}_{mix})^{simul} \tag{3.6}$$

In this way, other dynamical correlations -that are presented in both data and simulations not coming from Bose-Einstein- should cancel out. This procedure should also correct for other biases coming from efficiency/acceptance of the detector; violation of momentum energy conservation in the background distribution; particle misidentification; and selection cuts. The double ratio correlations obtained are shown in Fig. 3.15

3.3.5 Experimental Goldhaber Parametrization Fitting

In order to extract the parameters r and λ from the correlation function obtained, we need to fit the final shape. Different parametrizations can be used to fit the correlation function. Most applied functions found in literature and other studies [13], [15] [14] correspond to the Goldhaber parametrization presented in Eq. 1.23. The Golhaber parametrization is an approximation that considers the source of the pions as a perfect spherical Gaussian distribution, which in general is not the case. Additianaly, it does not take in consideration all other possible interaction between the pions, the source, and other generated particles in the process. In order to get adaptable function to adjust the shape of the experimental correlation function, the Goldhaber parametrization has to be multiplied by an additional polynomial to describe long-range correlations at larger values Q_{12}. An additional parameter γ is also included in the parametrization as a normalization factor. The experimental Golhaber parametrization will have the

following structure:

$$R(Q_{12}) = \gamma(1 + \lambda exp(-r^2 Q_{12}^2))(P(Q_{12})) \tag{3.7}$$

First, second and third order polynomials: $[1 + \delta(Q_{12})]$, $[1 + \delta(Q_{12}) + \epsilon(Q_{12}^2)]$ and $[1 + \delta(Q_{12}) + \epsilon(Q_{12}^2) + \sigma(Q_{12}^3)]$ were tested for the fit, where δ, ϵ and σ are free parameters.

The second order polynomial $[1 + \delta(Q_{12}) + \epsilon(Q_{12}^2)]$ was chosen for the final fit in this analysis mainly because it adjusted better to the shape with less free parameters, resulting in better χ^2/ndf among the nuclear targets. The specific parametrization to fit the correlation function used in analysis to get the r and λ has the following form:

$$R(Q_{12}) = \gamma(1 + \lambda exp(-r^2 Q_{12}^2))(1 + \delta(Q_{12}) + \epsilon(Q_{12}^2)) \tag{3.8}$$

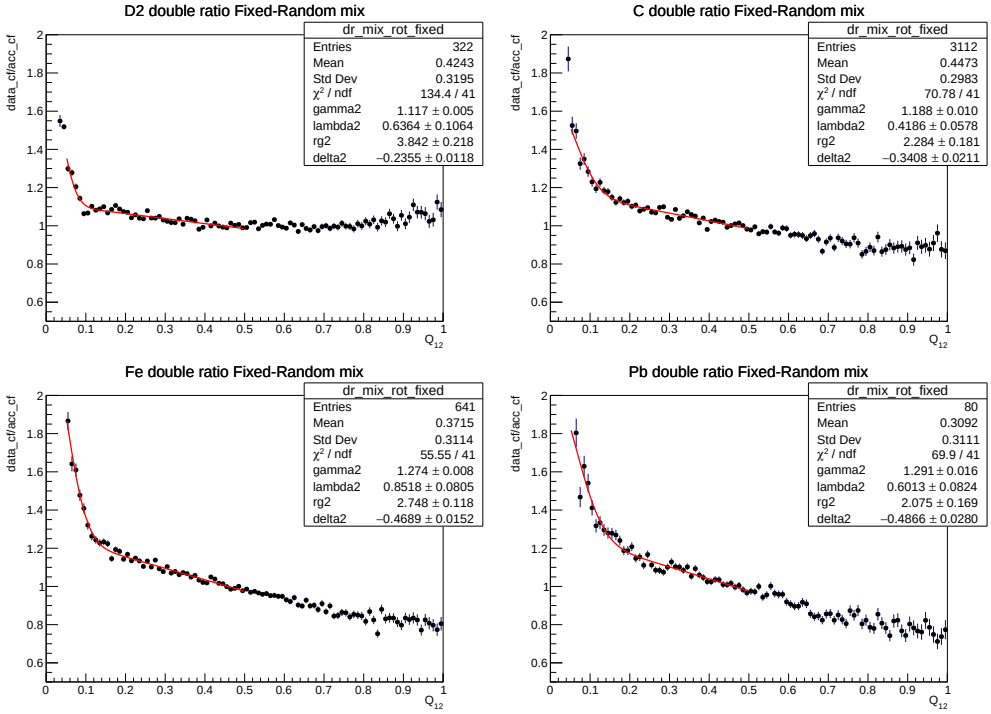

Figure 3.15: Double Ratio obtained by dividing the data correlation function by the simulated one for all four nuclear targets. Goldhaber fit applied is shown in red.

The parameters obtained in the fit for each target can be found in Table 3.5

Fit	Deuterium	Carbon	Iron	Lead
γ	1.142 ± 0.012	1.244 ± 0.035	1.313 ± 0.026	1.353 ± 0.082
λ	0.653 ± 0.122	0.427 ± 0.075	0.858 ± 0.088	0.616 ± 0.110
r	4.033 ± 0.252	2.577 ± 0.301	2.873 ± 0.150	2.280 ± 0.370
δ	-0.393 ± 0.069	-0.604 ± 0.156	-0.650 ± 0.110	-0729 ± 0.305
ϵ	0.263 ± 0.115	0.403 ± 0.242	0.293 ± 0.181	0.364 ± 0.460
χ^2/ndf	$129.5/40$	$68.53/40$	$53.18/40$	$69.39/40$

Table 3.5: Parameters obtained from the Goldhaber fit performed over all nuclear targets.

3.4 Two Dimensional Bose-Einstein Correlation

Up to this point in the analysis, we have described the Bose-Einstein correlation depending on $Q_{12} = (\sqrt{-(p_1 - p_2)^2})$ using one dimensional parametrization. This approach was based on the assumption that the pions's source density is a Gaussian distribution described with one spatial parameter r. This assumption leads to a perfect spherical geometry. Bose-Einstein correlations can also be studied in more than one dimensions to describe the shape of the bosonic source. Studies in two or three dimensions have been performed in other experiments to extract a more accurate picture of the bosonic source. With a two-dimensional approach, we can "see" the pion source with more detail by describing it with a spheroid-like shape that gives information about the elongation of the source. Therefore, the correlation function is parametrized using two space-time parameters. In DIS experiments, it is common to look at the longitudinal and transverse components of the pair's three-momentum difference, on respect to the virtual photon axis. We are looking for differences in the size of the source along these two perpendicular directions to see if the source is elongated along any of these two axes. Other studies in deep inelastic scattering experiments show an elongation along the longitudinal component of the source [33] [13].

For the two-dimensional case, instead of the Laboratory frame, the Longitudinally Co-Moving System (LCMS) is often used as system of reference. In the LCMS, Bose-Einstein correlations can be interpreted by the Lund-String Model [34][35] since it represents the local rest frame of a string. The LCMS is defined for each pair of particles with momenta $\overrightarrow{p}_1$ and $\overrightarrow{p}_2$, so that the sum of the momenta of both pions $\overrightarrow{p}_{12} = (\overrightarrow{p}_1 + \overrightarrow{p}_2)$ is perpendicular to the virtual photon axis. To accomplish this, a

Lorentz boost is applied in a pair to pair basis to meet the previous requirement.

In this system, we decompose the momenta difference $\overrightarrow{Q}_{12} = (\overrightarrow{p}_1 - \overrightarrow{p}_2)$ in its longitudinal and perpendicular components (q_l, q_t).

The two-dimensional analysis was performed in the same way to the one-dimensional study. The exact same pairs constructed in the one-dimensional study were used to build the signal and background distributions in the two-dimensional case with an additional cut: $Q_{12} < 0.05$. In this way, we are removing the same pairs not considered in the one-dimensional study because of Coulomb effects for close pion pairs. The two-dimensional correlation function is calculated:

$$R(Q_{12}) = R(q_l, q_t)^{data} / R(q_l, q_t)^{simul} \tag{3.9}$$

$$R(Q_{12}) = (\frac{D(q_l, q_t)}{D(q_l, q_t)}_{mix})^{data} / (\frac{D(q_l, q_t)}{D(q_l, q_t)}_{mix})^{simul} \tag{3.10}$$

In this case, a two-dimensional Goldhaber function can be applied to fit the Bose-Einstein effect. The parametrization, which already includes a normalization factor and a polynomial to describe long-range correlations, is written in the form:

$$R(q_l, q_t) = \gamma(1 + \delta_l q_l + \delta_t q_t)(1 + \lambda exp[-(r_l^2 q_l^2 + r_t^2 q_t^2)]) \tag{3.11}$$

where r_l and r_t can be interpreted as longitudinal and transverse size of the pion source, λ correspond to the coherence parameter. γ is a normalization factor. δ_l δ_t are free parameters.

In this case, the fits were performed in the range $0 < q_l < 0.5GeV$ and $0 < q_t < 0.5GeV$.

For the two-dimensional correlation plots (Fig. 3.16, 3.18, 3.20, 3.22), the strength of the correlation can be seen in the vertical axis, where an enhancement on the correlation function can be found near $q_l = q_t = 0$. In the upper side plot, a three dimensional view of the correlation shape is shown. The red surface represents the Goldhaber fit from Eq. 3.11 applied to the curve obtained. The lower side plot shows the same curve and fit seen from above; the red lines shows regions of fit with the same correlation strength value.

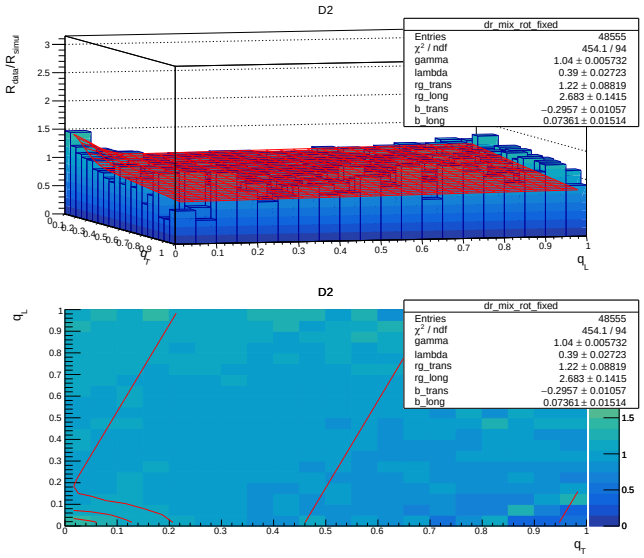

Figure 3.16: Two-dimensional correlation function for Deuterium target. In the top image, a 3D representation of the correlation function is show. At the top left corner, an enhancement in the distribution can be seen at $q_l = q_t = 0$. In the bottom image, a 2D projection can be seen with q_l and q_t in the vertical and horizontal axes respectively. The red curve shows the two-dimensional Goldhaber fit.

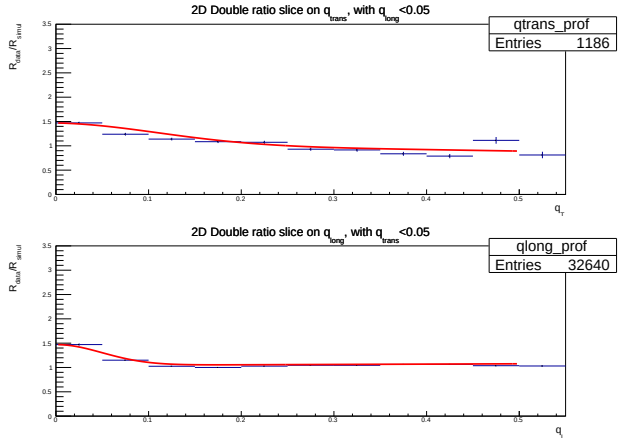

Figure 3.17: Two-dimensional correlation function slices for Deuterium target. In the top image the first bin on q_l ($0 < q_l < 0.05$) is shown, with q_t in the horizontal axis. The bottom image shows the first bin on q_t ($0 < q_t < 0.05$) is shown, with q_l in the horizontal axis. Red line shows the two-dimensional Goldhaber fit.

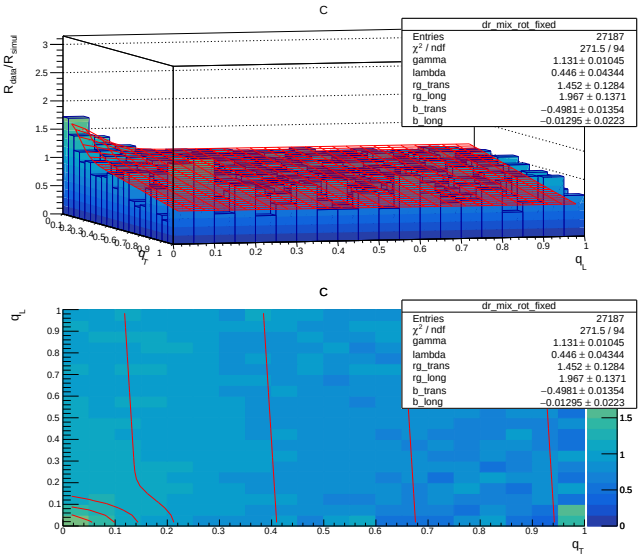

Figure 3.18: Two-dimensional correlation function for Carbon target. In the top image, a 3D representation of the correlation function is show. At the top left corner, an enhancement in the distribution can be seen at $q_l = q_t = 0$. In the bottom image, a 2D projection can be seen with q_l and q_t in the vertical and horizontal axes respectively. The red curve shows the two-dimensional Goldhaber fit.

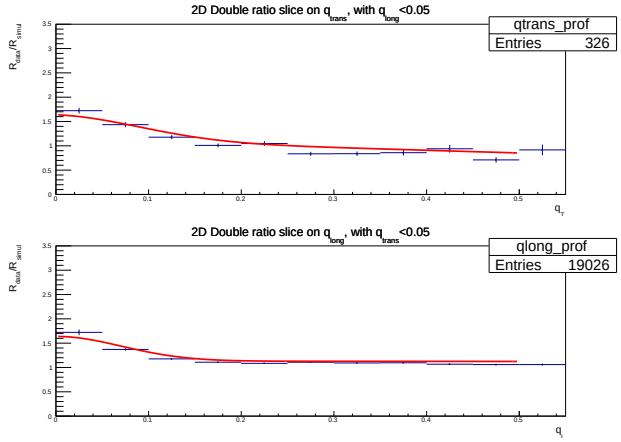

Figure 3.19: Two-dimensional correlation function slices for Carbon target. In the top image the first bin on q_l ($0 < q_l < 0.05$) is shown, with q_t in the horizontal axis. The bottom image shows the first bin on q_t ($0 < q_t < 0.05$) is shown, with q_l in the horizontal axis. Red line shows the two-dimensional Goldhaber fit.

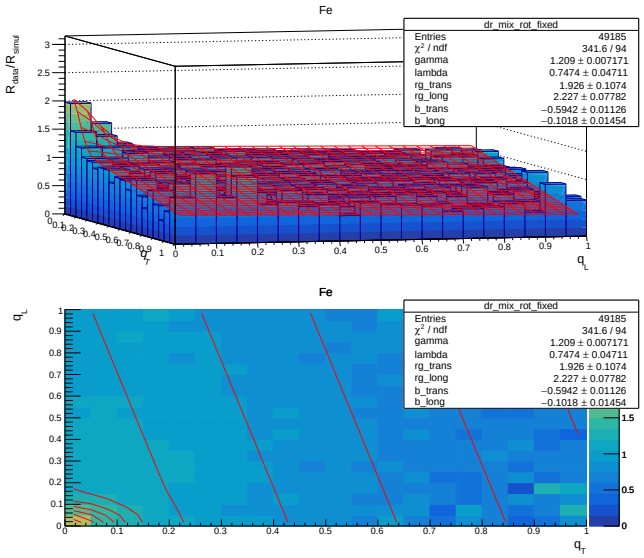

Figure 3.20: Two-dimensional correlation function for Iron target. In the top image, a 3D representation of the correlation function is show. At the top left corner, an enhancement in the distribution can be seen at $q_l = q_t = 0$. In the bottom image, a 2D projection can be seen with q_l and q_t in the vertical and horizontal axes respectively. The red curve shows the two-dimensional Goldhaber fit.

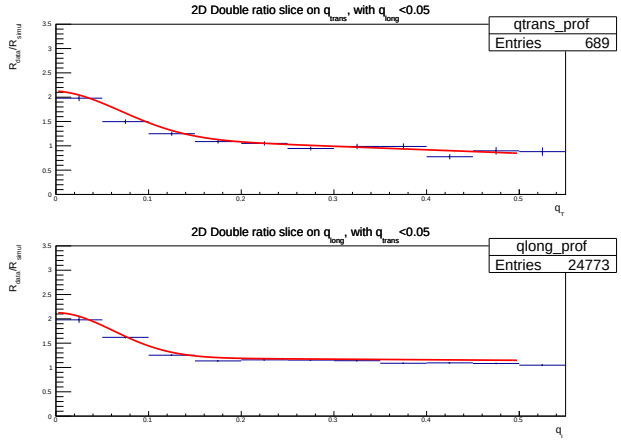

Figure 3.21: Two-dimensional correlation function slices for Iron target. In the top image the first bin on q_l ($0 < q_l < 0.05$) is shown, with q_t in the horizontal axis. The bottom image shows the first bin on q_t ($0 < q_t < 0.05$) is shown, with q_l in the horizontal axis. Red line shows the two-dimensional Goldhaber fit.

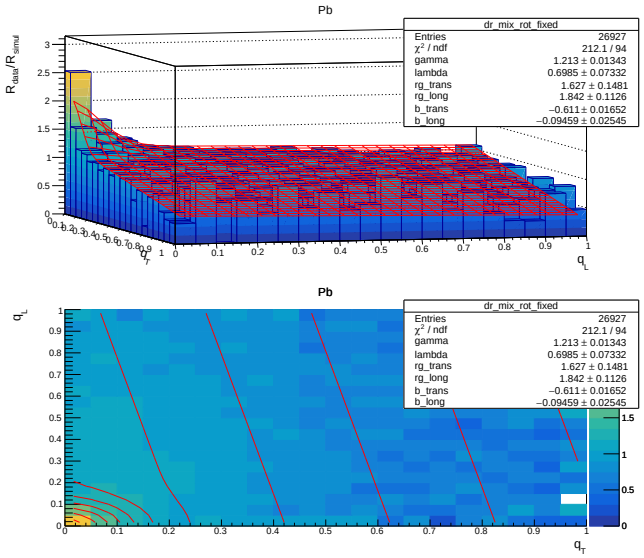

Figure 3.22: Two-dimensional correlation function for Lead target. In the top image, a 3D representation of the correlation function is show. At the top left corner, an enhancement in the distribution can be seen at $q_l = q_t = 0$. In the bottom image, a 2D projection can be seen with q_l and q_t in the vertical and horizontal axes respectively. The red curve shows the two-dimensional Goldhaber fit.

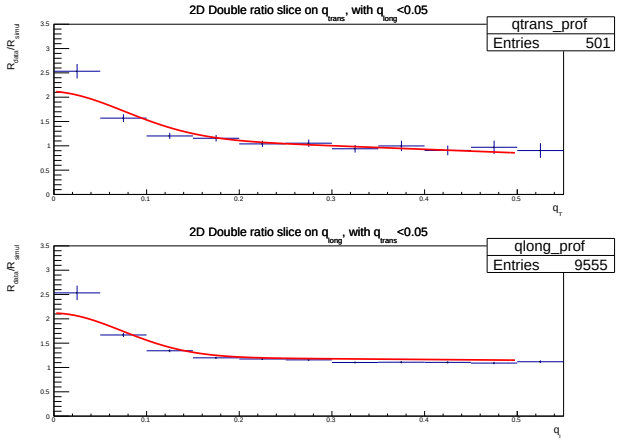

Figure 3.23: Two-dimensional correlation function slices for Lead target. In the top image the first bin on q_l ($0 < q_l < 0.05$) is shown, with q_t in the horizontal axis. The bottom image shows the first bin on q_t ($0 < q_t < 0.05$) is shown, with q_l in the horizontal axis. Red line shows the two-dimensional Goldhaber fit.

In order to visualize the results in an easier way, slice plots on the q_t and q_l variables of the two-dimensional correlations are presented in Fig. 3.17, 3.19, 3.21, 3.23. In the uppermost plots, the first bin of q_l of the correlation function is shown, corresponding to the pairs with $q_l < 0.05GeV$ and full range on q_t. In a similar way, on the lowermost plots, the correlation function is presented taking only the first bin on q_t which corresponds to the full range on q_l with $q_t < 0.05GeV$. The red curve in the slice plots shows the projection of the two-dimensional fit at $q_l = 0$ and $q_t = 0$ in the top and bottom plot respectively, and do not represent 1-dimensional fits.

3.5 Systematics

Systematic errors arise from the data's treatment. The different methods on processing the data can lead to deviations from the parameters values obtained for r, r_l, r_t, and λ in both one and two-dimensional analysis. In Bose-Einstein studies, the most important source of systematics comes from the construction of the background distribution. Different methods of event mixing could present different biases and thus different results. There is no "the" perfect method for the data mixing. Another important source systematic arises from the function chosen for the fit in order to get the parameters r, r_l, r_t and λ. Different fit functions and ranges of fitting could affect the final results. The way of binning the correlation function and the polynomial chosen for the parametrizations 3.7 and 3.11 are selected based on the best goodness of the fit among them, but the remaining polynomials are still valid options.

In order to estimate the uncertainty errors related to these factors, we repeated the analysis described previously with all possible combinations of different:

- Methods for the construction of the background distribution.
- Fit ranges
- Parametrization functions.
- Binning.

to get all the important parameters previously mentioned. We obtained slightly different results compared to the standard analysis. Then, we calculated the square root of the mean of squares (RMS) of the deviation of the modified parameters r, r_l, r_t and λ from the results calculated with standard method in the following way: $\Delta_{RMS} = \sqrt{\Sigma\Delta_n^2/n}$ where Δ is the difference between the parameter values obtained using the standard and the alternative method tested. n is the number of different methods in each systematic error estimation.

3.5.1 Mixing Procedure

Two different procedures were tested in order to do the mixing of events. This helped to check how the construction of the background affected the behaviour of the Q_{12} distribution of the mixed pairs and the final correlation function. The tested methods, that presented good results, are listed here:

- Fixed-Random: first pion of the pair is selected using the first pion in the dataset. The second pion of the first pair is chosen using a random number generator from an event different of the first one. Then, for the construction of the next pair, the first pion of the pair is chosen using the second pion in the dataset while the second pair is selected randomly from a different event and so on. This was the standard method used in the main analysis to create the pairs for the background distribution.

- Random-Random: for each pair, the first and second pions are selected from different events using two different random generated numbers.

The systematic errors estimated from the mixing procedure of the background distribution can be summarized in the following tables. In Tables 3.6, and 3.7 the systematic errors for the parameters r and λ in the one-dimensional and two-dimensional analysis respectively are presented for all four different nuclear targets.

Target	r	λ
D2	$\pm 0.124(3.07\%)$	$\pm 0.056(8.55\%)$
C	$\pm 0.089(3.43\%)$	$\pm 0.014(3.31\%)$
Fe	$\pm 0.141(4.90\%)$	$\pm 0.022(2.56\%)$
Pb	$\pm 0.116(5.11\%)$	$\pm 0.016(2.62\%)$

Table 3.6: Systematic errors estimated from the mixing method on the background distribution construction in the one-dimensional analysis.

Target	r_t	r_l	r_t/r_l	λ
D2	$\pm 0.037(3.07\%)$	$\pm 0.140(5.22\%)$	$\pm 0.028(6.12\%)$	$\pm 0.024(6.04\%)$
C	$\pm 0.041(2.85\%)$	$\pm 0.031(1.60\%)$	$\pm 0.014(1.92\%)$	$\pm 0.004(0.97\%)$
Fe	$\pm 0.049(2.54\%)$	$\pm 0.017(0.78\%)$	$\pm 0.022(2.60\%)$	$\pm 0.017(2.30\%)$
Pb	$\pm 0.091(5.56\%)$	$\pm 0.037(2.02\%)$	$\pm 0.036(4.14\%)$	$\pm 0.029(4.21\%)$

Table 3.7: Systematic errors estimated from the mixing method on the background distribution construction in the two-dimensional analysis.

3.5.2 Fitting

Alternatives functions to the fitting parametrization presented in Eq. 3.7 were tested to fit the final correlation functions. In the one-dimensional analysis, we tried the Goldhaber parametrization using first order and third order polynomials to fit the tail of the correlation:

$$R(Q_{12}) = \gamma(1 + \lambda exp(-r^2 Q_{12}^2))(1 + \delta(Q_{12})) \tag{3.12}$$

$$R(Q_{12}) = \gamma(1 + \lambda exp(-r^2 Q_{12}^2))(1 + \delta(Q_{12}) + \epsilon(Q_{12}^2 + \sigma(Q_{12}^3))) \tag{3.13}$$

In a similar way for the two-dimensional case, an alternative parametrization to the function presented in Eq. 3.11 was tested, which consists on a second order polynomial

to fit the two dimensional tail of the correlation:

$$R(q_l, q_t) = \gamma(1 + \lambda exp[-(r_l^2 q_l^2 + r_t^2 q_t^2)](1 + \delta_l q_l + \delta_t q_t + \epsilon q_t q_l + \sigma_l q_l^2 + \sigma_t q_t^2) \quad (3.14)$$

In the one-dimensional case, the same parametrization functions were applied to fit the correlation distribution constructed with variable bin sizes instead of equally sized bins. We used thinner bins in the correlation for smaller values of Q_{12} where the shape of the correlation is steeper and has more importance than the tail, where the enhancement is smaller.

The estimated errors for r, r_t, r_l, and λ, related to the fitting function applied and binning, are found in Tables 3.8, 3.9, and 3.10:

Target	r	λ
D2	$\pm 0.238(5.90\%)$	$\pm 0.051(7.86\%)$
C	$\pm 0.384(14.90\%)$	$\pm 0.017(3.90\%)$
Fe	$\pm 0.133(4.64\%)$	$\pm 0.020(2.36\%)$
Pb	$\pm 0.272(11.91\%)$	$\pm 0.024(3.79\%)$

Table 3.8: Systematic errors estimated from the parametrization function chosen for the fit in the one-dimensional study.

Target	r_t	r_l	r_t/r_l	λ
D2	$\pm 0.220(18.03\%)$	$\pm 0.655(24.43\%)$	$\pm 0.025(5.45\%)$	$\pm 0.010(2.48\%)$
C	$\pm 0.146(10.10\%)$	$\pm 0.207(10.48\%)$	$\pm 0.029(3.86\%)$	$\pm 0.030(6.73\%)$
Fe	$\pm 0.084(4.36\%)$	$\pm 0.120(5.36\%)$	$\pm 0.016(1.91\%)$	$\pm 0.032(4.32\%)$
Pb	$\pm 0.183(11.25\%)$	$\pm 0.175(9.50\%)$	$\pm 0.035(4.01\%)$	$\pm 0.064(9.20\%)$

Table 3.9: Systematic errors estimated from the parametrization function chosen for the fit in the two-dimensional study.

Target	r	λ
D2	$\pm 0.258(6.40\%)$	$\pm 0.031(4.71\%)$
C	$\pm 0.177(6.87\%)$	$\pm 0.013(3.07\%)$
Fe	$\pm 0.049(1.70\%)$	$\pm 0.033(3.81\%)$
Pb	$\pm 0.097(4.26\%)$	$\pm 0.022(3.50\%)$

Table 3.10: Systematic errors estimated from the binning used for the construction of correlation function.

3.5.3 Fit range

Three different ranges for the fit on Q_{12} were tested in the one-dimensional study: $0.05 < Q_{12} < 0.50$, $0.05 < Q_{12} < 1.00$, $0.05 < Q_{12} < 1.50$. On the other hand, in the two-dimensional case the ranges tested for the variables q_t and q_l are: $0.05 < q_i < 0.50$, $0.05 < q_i < 0.75$, $0.05 < q_i < 1.00$, where $i = t, l$. The systematic errors estimated from range on the fitting can be summarized in the following tables. In Table 3.11, the systematic errors for the parameters r and λ in the one-dimensional analysis. In Table 3.12, the systematic errors for the parameters r_l, r_t and λ in the two-dimensional analysis.

Target	r	λ
D2	$\pm 0.137(3.35\%)$	$\pm 0.035(5.30\%)$
C	$\pm 0.301(12.32\%)$	$\pm 0.020(4.67\%)$
Fe	$\pm 0.176(6.20\%)$	$\pm 0.048(5.77\%)$
Pb	$\pm 0.262(12.03\%)$	$\pm 0.041(7.05\%)$

Table 3.11: Systematic errors estimated from the fit range in the correlation function in the one-dimensional case.

3.5.4 Total Errors

The systematic errors estimated from all sources previously discussed were added in quadrature. The total errors for one and two dimensional studies are presented in Tables 3.13 and 3.14 respectively.

Target	r_t	r_l	r_t/r_l	λ
D2	$\pm 0.063(5.20\%)$	$\pm 0.191(7.11\%)$	$\pm 0.013(2.93\%)$	$\pm 0.012(3.12\%)$
C	$\pm 0.069(4.78\%)$	$\pm 0.063(3.17\%)$	$\pm 0.026(3.50\%)$	$\pm 0.018(4.04\%)$
Fe	$\pm 0.047(2.41\%)$	$\pm 0.052(2.33\%)$	$\pm 0.009(1.02\%)$	$\pm 0.027(3.54\%)$
Pb	$\pm 0.057(3.47\%)$	$\pm 0.079(4.30\%)$	$\pm 0.025(2.83\%)$	$\pm 0.021(3.07\%)$

Table 3.12: Systematic errors estimated from the fit range in the correlation function in the two-dimensional case.

Target	r	λ
D2	$\pm 0.037(9.1\%)$	$\pm 0.08(12.3\%)$
C	$\pm 0.043(16.7\%)$	$\pm 0.03(7.0\%)$
Fe	$\pm 0.020(7.0\%)$	$\pm 0.04(4.65\%)$
Pb	$\pm 0.031(13.6\%)$	$\pm 0.04(6.45\%)$

Table 3.13: Total systematic errors estimated in the one-dimensional study.

Target	r_t	r_l	r_t/r_l	λ
D2	$\pm 0.23(18.6\%)$	$\pm 0.70(26.1\%)$	$\pm 0.04(8.9\%)$	$\pm 0.03(7.7\%)$
C	$\pm 0.17(11.7\%)$	$\pm 0.22(11.2\%)$	$\pm 0.08(5.4\%)$	$\pm 0.04(8.9\%)$
Fe	$\pm 0.11(5.7\%)$	$\pm 0.13(5.8\%)$	$\pm 0.06(3.5\%)$	$\pm 0.05(6.7\%)$
Pb	$\pm 0.21(12.9\%)$	$\pm 0.20(12.3\%)$	$\pm 0.10(6.8\%)$	$\pm 0.07(10.0\%)$

Table 3.14: Total systematic errors estimated in the two-dimensional study.

3.5.5 Comparison Tables

The fit parameters λ and r measured with all possible combinations of: event mixing methods, fit functions, fit ranges and binning are presented in Tables 3.15, 3.16, 3.17, 3.18 for the one-dimesional study and Tables 3.19, 3.20, 3.21, 3.22 for the two-dimensional case.

Results from all different presented methods show relative small difference in the final parameters obtained. Bigger differences arise from the parametrization function which is chosen for the fit in comparison to the mixing technique used to construct the

background distribution. Fitting for lead target presents problems when using third-order polynomial on the fit of the correlation function, and was removed to the calculation of systematic errors only for that target.

			$0.05 < Q_{12} < 0.50$			$0.05 < Q_{12} < 1.00$			$0.05 < Q_{12} < 1.50$		
Method	Fit function	Binning	r	λ	chi^2/ndf	r	λ	chi^2/ndf	r	λ	chi^2/ndf
Fixed-Random			4.03 ± 0.25	0.65 ± 0.12	3.24	4.09 ± 0.25	0.66 ± 0.13	2.09	4.06 ± 0.24	0.65 ± 0.12	1.53
		Variable bin	3.71 ± 0.11	0.65 ± 0.05	13.93	3.73 ± 0.11	0.65 ± 0.05	12.42	3.61 ± 0.10	0.64 ± 0.05	13.04
Random-Random	2st order pol		3.92 ± 0.24	0.60 ± 0.11	3.00	3.89 ± 0.23	0.60 ± 0.10	1.89	3.86 ± 0.22	0.60 ± 0.10	1.44
		Variable bin	3.72 ± 0.13	0.59 ± 0.05	11.67	3.69 ± 0.12	0.59 ± 0.05	10.41	3.55 ± 0.11	0.58 ± 0.05	11.15
Fixed-Random			3.84 ± 0.22	0.64 ± 0.11	3.28	3.01 ± 0.22	0.47 ± 0.07	4.58	0.74 ± 0.04	0.21 ± 0.01	3.23
		Variable bin	3.59 ± 0.10	0.65 ± 0.05	13.20	3.22 ± 0.10	0.59 ± 0.04	28.19	3.01 ± 0.10	0.55 ± 0.04	52.92
Random-Random	1st order pol		3.64 ± 0.20	0.59 ± 0.09	3.19	2.78 ± 0.22	0.43 ± 0.06	4.23	0.81 ± 0.04	0.21 ± 0.01	3.27
		Variable bin	3.52 ± 0.11	0.59 ± 0.05	11.91	3.08 ± 0.11	0.52 ± 0.04	26.05	2.81 ± 0.12	0.47 ± 0.04	51.39
Fixed-Random			3.79 ± 0.24	0.68 ± 0.10	3.17	4.01 ± 0.25	0.65 ± 0.12	2.10	4.10 ± 0.25	0.66 ± 0.13	1.54
		Variable bin	3.46 ± 0.11	0.75 ± 0.05	12.66	3.67 ± 0.12	0.66 ± 0.05	13.72	3.75 ± 0.11	0.65 ± 0.05	12.60
Random-Random	3rd order pol		3.63 ± 0.23	0.64 ± 0.09	2.85	3.84 ± 0.23	0.60 ± 0.10	1.90	3.92 ± 0.24	0.60 ± 0.11	1.44
		Variable bin	3.44 ± 0.13	0.67 ± 0.05	10.64	3.68 ± 0.13	0.59 ± 0.05	11.70	3.72 ± 0.13	0.59 ± 0.05	10.47

Table 3.15: One-dimensional study - Deuterium Target.

			$0.05 < Q_{12} < 0.50$			$0.05 < Q_{12} < 1.00$			$0.05 < Q_{12} < 1.50$		
Method	Fit function	Binning	r	λ	chi^2/ndf	r	λ	chi^2/ndf	r	λ	chi^2/ndf
Fixed-Random			2.58 ± 0.30	0.43 ± 0.08	1.71	2.44 ± 0.20	0.43 ± 0.07	1.42	2.44 ± 0.20	0.43 ± 0.07	1.16
		Variable bin	2.72 ± 0.30	0.43 ± 0.07	2.37	2.46 ± 0.20	0.42 ± 0.06	2.33	2.26 ± 0.15	0.40 ± 0.05	2.43
Random-Random	2st order pol		2.52 ± 0.29	0.43 ± 0.08	1.53	2.52 ± 0.21	0.44 ± 0.07	1.22	2.53 ± 0.20	0.44 ± 0.07	0.98
		Variable bin	2.54 ± 0.27	0.42 ± 0.06	3.21	2.48 ± 0.20	0.42 ± 0.06	2.87	2.31 ± 0.15	0.40 ± 0.05	2.87
Fixed-Random			2.28 ± 0.18	0.42 ± 0.06	1.73	2.02 ± 0.14	0.39 ± 0.05	1.60	1.86 ± 0.13	0.37 ± 0.04	1.52
		Variable bin	2.27 ± 0.16	0.41 ± 0.05	2.67	1.94 ± 0.11	0.38 ± 0.04	4.01	1.65 ± 0.10	0.34 ± 0.03	12.09
Random-Random	1st order pol		2.36 ± 0.19	0.43 ± 0.06	1.52	2.08 ± 0.15	0.39 ± 0.05	1.43	1.91 ± 0.13	0.37 ± 0.04	1.38
		Variable bin	2.32 ± 0.16	0.41 ± 0.05	3.01	1.98 ± 0.12	0.38 ± 0.04	4.47	1.69 ± 0.10	0.34 ± 0.03	12.86
Fixed-Random			2.91 ± 0.54	0.41 ± 0.10	1.74	2.31 ± 0.23	0.42 ± 0.06	1.42	2.43 ± 0.22	0.42 ± 0.07	1.17
		Variable bin	3.20 ± 0.55	0.43 ± 0.11	2.50	2.86 ± 0.36	0.43 ± 0.08	2.30	2.51 ± 0.22	0.42 ± 0.06	2.28
Random-Random	3rd order pol		2.85 ± 0.53	0.40 ± 0.10	1.55	2.33 ± 0.23	0.43 ± 0.06	1.21	2.47 ± 0.22	0.43 ± 0.07	0.98
		Variable bin	3.20 ± 0.59	0.40 ± 0.11	3.34	2.62 ± 0.33	0.42 ± 0.07	3.18	2.52 ± 0.22	0.42 ± 0.06	2.85

Table 3.16: One-dimensional study - Carbon Target.

			$0.05 < Q_{12} < 0.50$			$0.05 < Q_{12} < 1.00$			$0.05 < Q_{12} < 1.50$		
Method	Fit function	Binning	r	λ	chi^2/ndf	r	λ	chi^2/ndf	r	λ	chi^2/ndf
Fixed-Random			2.87 ± 0.15	0.86 ± 0.09	1.33	2.83 ± 0.12	0.86 ± 0.08	1.14	2.81 ± 0.12	0.85 ± 0.08	0.98
		Variable bin	2.87 ± 0.13	0.84 ± 0.08	1.02	2.84 ± 0.12	0.84 ± 0.08	0.93	2.64 ± 0.10	0.80 ± 0.07	2.52
Random-Random	2st order pol		2.95 ± 0.16	0.89 ± 0.10	1.54	2.86 ± 0.13	0.88 ± 0.09	1.15	2.83 ± 0.13	0.87 ± 0.09	1.03
		Variable bin	2.94 ± 0.15	0.85 ± 0.09	1.65	2.89 ± 0.13	0.84 ± 0.09	1.51	2.63 ± 0.10	0.78 ± 0.07	3.54
Fixed-Random			2.75 ± 0.12	0.85 ± 0.08	1.35	2.52 ± 0.10	0.79 ± 0.07	1.55	2.37 ± 0.10	0.75 ± 0.06	1.74
		Variable bin	2.71 ± 0.10	0.83 ± 0.07	1.42	2.38 ± 0.09	0.74 ± 0.06	7.07	2.09 ± 0.08	0.65 ± 0.05	25.15
Random-Random	1st order pol		2.80 ± 0.13	0.87 ± 0.09	1.58	2.54 ± 0.11	0.80 ± 0.07	1.54	2.39 ± 0.10	0.75 ± 0.07	1.71
		Variable bin	2.73 ± 0.11	0.82 ± 0.07	2.12	2.35 ± 0.09	0.71 ± 0.06	8.20	2.03 ± 0.09	0.61 ± 0.05	24.33
Fixed-Random			2.95 ± 0.20	0.83 ± 0.09	1.35	2.79 ± 0.14	0.85 ± 0.08	1.15	2.86 ± 0.13	0.86 ± 0.09	0.98
		Variable bin	2.87 ± 0.18	0.84 ± 0.09	1.16	2.88 ± 0.14	0.83 ± 0.08	1.02	2.87 ± 0.11	0.83 ± 0.07	0.90
Random-Random	3rd order pol		3.16 ± 0.24	0.86 ± 0.12	1.52	2.89 ± 0.15	0.88 ± 0.09	1.16	2.92 ± 0.15	0.89 ± 0.10	1.02
		Variable bin	3.12 ± 0.22	0.82 ± 0.10	1.62	2.97 ± 0.17	0.84 ± 0.09	1.61	2.93 ± 0.13	0.84 ± 0.09	1.45

Table 3.17: One-dimensional study - Iron Target.

			$0.05 < Q_{12} < 0.50$			$0.05 < Q_{12} < 1.00$			$0.05 < Q_{12} < 1.50$		
Method	Fit function	Binning	r	λ	chi^2/ndf	r	λ	chi^2/ndf	r	λ	chi^2/ndf
Fixed-Random			2.28 ± 0.37	0.62 ± 0.11	1.73	2.22 ± 0.19	0.62 ± 0.10	1.44	2.19 ± 0.17	0.61 ± 0.09	1.24
		Variable bin	2.46 ± 0.43	0.62 ± 0.14	6.80	2.18 ± 0.22	0.58 ± 0.09	6.12	1.96 ± 0.14	0.55 ± 0.07	5.77
Random-Random	2st order pol		2.46 ± 0.37	0.65 ± 0.14	1.69	2.22 ± 0.19	0.61 ± 0.10	1.44	2.22 ± 0.18	0.61 ± 0.10	1.26
		Variable bin	2.42 ± 0.37	0.61 ± 0.12	6.25	2.31 ± 0.22	0.60 ± 0.10	5.57	2.00 ± 0.14	0.55 ± 0.07	5.59
Fixed-Random			2.07 ± 0.17	0.60 ± 0.08	1.70	1.93 ± 0.13	0.57 ± 0.07	1.53	1.77 ± 0.11	0.54 ± 0.06	1.48
		Variable bin	2.02 ± 0.16	0.57 ± 0.07	6.22	1.74 ± 0.10	0.53 ± 0.05	6.57	1.43 ± 0.08	0.47 ± 0.04	13.78
Random-Random	1st order pol		2.15 ± 0.18	0.61 ± 0.09	1.68	1.95 ± 0.13	0.56 ± 0.07	1.51	1.77 ± 0.12	0.52 ± 0.06	1.50
		Variable bin	2.12 ± 0.17	0.59 ± 0.08	5.67	1.76 ± 0.11	0.52 ± 0.05	6.70	1.41 ± 0.09	0.45 ± 0.04	13.78
Fixed-Random			4.95 ± 0.25	2.00 ± 1.77	1.39	1.95 ± 0.19	0.62 ± 0.07	1.42	2.31 ± 0.22	0.63 ± 0.10	1.24
		Variable bin	5.10 ± 0.26	2.00 ± 1.41	4.93	3.02 ± 0.56	0.72 ± 0.24	6.47	2.24 ± 0.24	0.58 ± 0.10	6.09
Random-Random	3rd order pol		4.88 ± 0.24	2.00 ± 1.55	1.38	2.13 ± 0.24	0.61 ± 0.09	1.45	2.32 ± 0.23	0.63 ± 0.11	1.26
		Variable bin	5.07 ± 0.26	2.00 ± 1.30	4.42	2.81 ± 0.54	0.67 ± 0.20	6.09	2.38 ± 0.25	0.61 ± 0.11	5.53

Table 3.18: One-dimensional study - Lead Target.

Fit Range	Mixing	Fit Function	r_t	r_l	r_t/r_l	λ	chi^2/ndf
	Fixed-Random	1st order pol	1.22 ± 0.09	2.68 ± 0.14	0.45 ± 0.04	0.39 ± 0.03	4.83
$0.00 < q_t < 0.50$	Random-Random	1st order pol	1.23 ± 0.08	2.82 ± 0.14	0.44 ± 0.04	0.41 ± 0.03	4.67
$0.00 < q_l < 0.50$	Fixed-Random	2nd order pol	1.35 ± 0.15	2.91 ± 0.19	0.47 ± 0.06	0.39 ± 0.03	4.39
	Random-Random	2nd order pol	1.27 ± 0.12	2.97 ± 0.17	0.43 ± 0.05	0.41 ± 0.03	4.37
	Fixed-Random	1st order pol	1.17 ± 0.07	2.48 ± 0.13	0.47 ± 0.04	0.38 ± 0.03	3.02
$0.00 < q_t < 0.75$	Random-Random	1st order pol	1.17 ± 0.07	2.64 ± 0.13	0.44 ± 0.03	0.41 ± 0.03	3.03
$0.00 < q_l < 0.75$	Fixed-Random	2nd order pol	1.34 ± 0.12	2.98 ± 0.16	0.45 ± 0.05	0.38 ± 0.03	2.73
	Random-Random	2nd order pol	1.30 ± 0.11	3.07 ± 0.16	0.42 ± 0.04	0.40 ± 0.03	2.74
	Fixed-Random	1st order pol	1.06 ± 0.06	2.18 ± 0.12	0.48 ± 0.04	0.36 ± 0.02	2.43
$0.00 < q_t < 1.00$	Random-Random	1st order pol	1.08 ± 0.06	2.36 ± 0.12	0.46 ± 0.04	0.39 ± 0.03	2.43
$0.00 < q_l < 1.00$	Fixed-Random	2nd order pol	1.38 ± 0.13	3.06 ± 0.17	0.45 ± 0.05	0.38 ± 0.03	2.06
	Random-Random	2nd order pol	1.34 ± 0.12	3.17 ± 0.16	0.42 ± 0.04	0.39 ± 0.03	2.04

Table 3.19: Two-dimensional study - Deuterium Target.

Fit Range	Mixing	Fit Function	r_t	r_l	r_t/r_l	λ	chi^2/ndf
	Fixed-Random	1st order pol	1.45 ± 0.13	1.97 ± 0.14	0.74 ± 0.08	0.45 ± 0.04	2.89
$0.00 < q_t < 0.50$	Random-Random	1st order pol	1.48 ± 0.13	1.98 ± 0.14	0.75 ± 0.08	0.45 ± 0.04	2.66
$0.00 < q_l < 0.50$	Fixed-Random	2nd order pol	1.66 ± 0.17	2.14 ± 0.18	0.78 ± 0.10	0.49 ± 0.05	1.95
	Random-Random	2nd order pol	1.64 ± 0.17	2.09 ± 0.17	0.79 ± 0.10	0.49 ± 0.05	1.78
	Fixed-Random	1st order pol	1.43 ± 0.12	1.92 ± 0.13	0.74 ± 0.08	0.44 ± 0.04	2.34
$0.00 < q_t < 0.75$	Random-Random	1st order pol	1.47 ± 0.12	1.95 ± 0.12	0.76 ± 0.08	0.44 ± 0.04	2.16
$0.00 < q_l < 0.75$	Fixed-Random	2nd order pol	1.50 ± 0.15	2.06 ± 0.16	0.73 ± 0.09	0.46 ± 0.05	1.85
	Random-Random	2nd order pol	1.55 ± 0.15	2.09 ± 0.15	0.74 ± 0.09	0.46 ± 0.05	1.70
	Fixed-Random	1st order pol	1.37 ± 0.11	1.82 ± 0.12	0.75 ± 0.08	0.42 ± 0.04	1.78
$0.00 < q_t < 1.00$	Random-Random	1st order pol	1.42 ± 0.11	1.86 ± 0.12	0.76 ± 0.08	0.43 ± 0.04	1.70
$0.00 < q_l < 1.00$	Fixed-Random	2nd order pol	1.52 ± 0.15	2.11 ± 0.16	0.72 ± 0.09	0.45 ± 0.05	1.56
	Random-Random	2nd order pol	1.57 ± 0.15	2.12 ± 0.15	0.74 ± 0.09	0.45 ± 0.05	1.51

Table 3.20: Two-dimensional study - Carbon Target.

Fit Range	Mixing	Fit Function	r_t	r_l	r_t/r_l	λ	chi^2/ndf
	Fixed-Random	1st order pol	1.93 ± 0.11	2.23 ± 0.08	0.86 ± 0.06	0.75 ± 0.05	3.63
$0.00 < q_t < 0.50$	Random-Random	1st order pol	1.90 ± 0.11	2.25 ± 0.08	0.85 ± 0.06	0.76 ± 0.05	3.55
$0.00 < q_l < 0.50$	Fixed-Random	2nd order pol	1.91 ± 0.12	2.21 ± 0.08	0.86 ± 0.06	0.80 ± 0.05	2.39
	Random-Random	2nd order pol	1.82 ± 0.11	2.23 ± 0.08	0.82 ± 0.06	0.82 ± 0.05	2.45
	Fixed-Random	1st order pol	1.90 ± 0.10	2.18 ± 0.08	0.87 ± 0.06	0.74 ± 0.05	2.63
$0.00 < q_t < 0.75$	Random-Random	1st order pol	1.87 ± 0.10	2.19 ± 0.07	0.85 ± 0.05	0.76 ± 0.05	2.54
$0.00 < q_l < 0.75$	Fixed-Random	2nd order pol	1.95 ± 0.12	2.26 ± 0.08	0.86 ± 0.06	0.75 ± 0.05	1.94
	Random-Random	2nd order pol	1.90 ± 0.11	2.27 ± 0.08	0.84 ± 0.06	0.77 ± 0.05	1.93
	Fixed-Random	1st order pol	1.85 ± 0.10	2.11 ± 0.07	0.87 ± 0.06	0.73 ± 0.05	2.33
$0.00 < q_t < 1.00$	Random-Random	1st order pol	1.82 ± 0.09	2.13 ± 0.07	0.86 ± 0.05	0.75 ± 0.05	2.20
$0.00 < q_l < 1.00$	Fixed-Random	2nd order pol	1.97 ± 0.12	2.29 ± 0.08	0.86 ± 0.06	0.74 ± 0.05	1.89
	Random-Random	2nd order pol	1.94 ± 0.11	2.31 ± 0.08	0.84 ± 0.06	0.75 ± 0.05	1.77

Table 3.21: Two-dimensional study - Iron Target.

Fit Range	Mixing	Fit Function	r_t	r_l	r_t/r_l	λ	chi^2/ndf
	Fixed-Random	1st order pol	1.63 ± 0.15	1.84 ± 0.11	0.88 ± 0.10	0.70 ± 0.07	2.26
$0.00 < q_t < 0.50$	Random-Random	1st order pol	1.75 ± 0.16	1.89 ± 0.12	0.92 ± 0.10	0.73 ± 0.08	2.07
$0.00 < q_l < 0.50$	Fixed-Random	2nd order pol	1.76 ± 0.18	1.87 ± 0.13	0.94 ± 0.12	0.77 ± 0.08	1.54
	Random-Random	2nd order pol	1.89 ± 0.20	1.93 ± 0.14	0.98 ± 0.12	0.80 ± 0.08	1.41
	Fixed-Random	1st order pol	1.66 ± 0.15	1.89 ± 0.11	0.88 ± 0.09	0.69 ± 0.08	2.45
$0.00 < q_t < 0.75$	Random-Random	1st order pol	1.72 ± 0.15	1.90 ± 0.11	0.91 ± 0.10	0.72 ± 0.08	2.46
$0.00 < q_l < 0.75$	Fixed-Random	2nd order pol	1.76 ± 0.18	1.98 ± 0.14	0.89 ± 0.11	0.74 ± 0.08	1.82
	Random-Random	2nd order pol	1.85 ± 0.18	2.00 ± 0.13	0.93 ± 0.11	0.77 ± 0.09	1.79
	Fixed-Random	1st order pol	1.55 ± 0.13	1.76 ± 0.10	0.88 ± 0.09	0.66 ± 0.07	2.11
$0.00 < q_t < 1.00$	Random-Random	1st order pol	1.63 ± 0.14	1.80 ± 0.10	0.91 ± 0.09	0.69 ± 0.07	2.14
$0.00 < q_l < 1.00$	Fixed-Random	2nd order pol	1.82 ± 0.19	2.06 ± 0.14	0.88 ± 0.11	0.73 ± 0.10	1.82
	Random-Random	2nd order pol	1.88 ± 0.19	2.05 ± 0.13	0.92 ± 0.11	0.76 ± 0.09	1.85

Table 3.22: Two-dimensional study - Lead Target.

Chapter 4

Results

4.1 One Dimensional Study

Correlation parameters r and λ were obtained from the fitting of the correlation function for each target using the experimental Goldhaber parametrization presented in section 3.3.5. The fit was performed in the range of $Q_{12} = [0.05 - 1.00]$ GeV. For Q_{12} values below this range, Coulomb interactions between pions become stronger and can not be neglected. Corrections must be applied to include lower values of Q_{12} in the fit. Coulomb corrections are not included in this analysis. Over $Q_{12} = 1.0$ GeV, the main Gaussian shape, which contains the pion source information, is diminished almost completely because its exponential nature, and only remains the linear long-range correlations tail. The values for λ and r measured for different nuclear targets are presented in Table 4.1.

Target	r [fm]	λ
D2	$4.03 \pm 0.25 \pm 0.21$	$0.65 \pm 0.12 \pm 0.05$
C	$2.58 \pm 0.30 \pm 0.25$	$0.43 \pm 0.08 \pm 0.01$
Fe	$2.87 \pm 0.15 \pm 0.12$	$0.86 \pm 0.09 \pm 0.03$
Pb	$2.28 \pm 0.37 \pm 0.18$	$0.62 \pm 0.11 \pm 0.02$

Table 4.1: Parameters obtained from Goldhaber fit. λ and r parameters represent coherence and size of the pion source respectively.

The parameters presented include statistical and systematic errors estimated in Section 3.5.

4.1.1 Nuclear Target Comparison

In Fig. 4.1, we can see the coherence parameter λ for each nuclear target.

By looking at the source radius parameter r in Figure 4.2, we can notice that the source' size remains constant within errors for all solid targets. A value of around 2.4 [fm] is measured among solid targets. Deuterium presents a different behavior when compared to other nuclei in the source size parameter r. For Deuterium target the radius measured is around 4.0 [fm].

The different behaviour between liquid and solid targets could come from ...

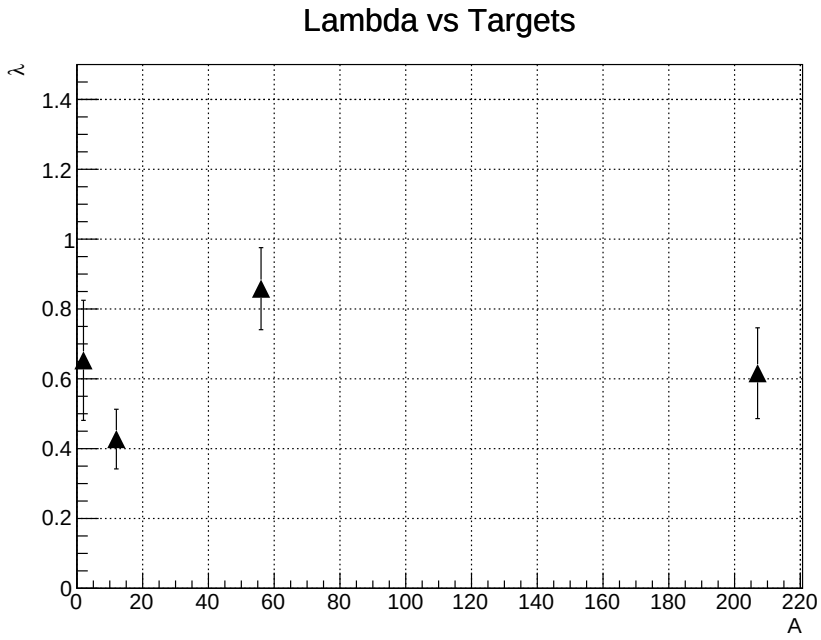

Figure 4.1: Coherence parameter λ vs nuclear mass number A in one-dimensional study. Nuclear target presented are: D2, C, Fe, Pb. This plot includes statistic and systematic errors.

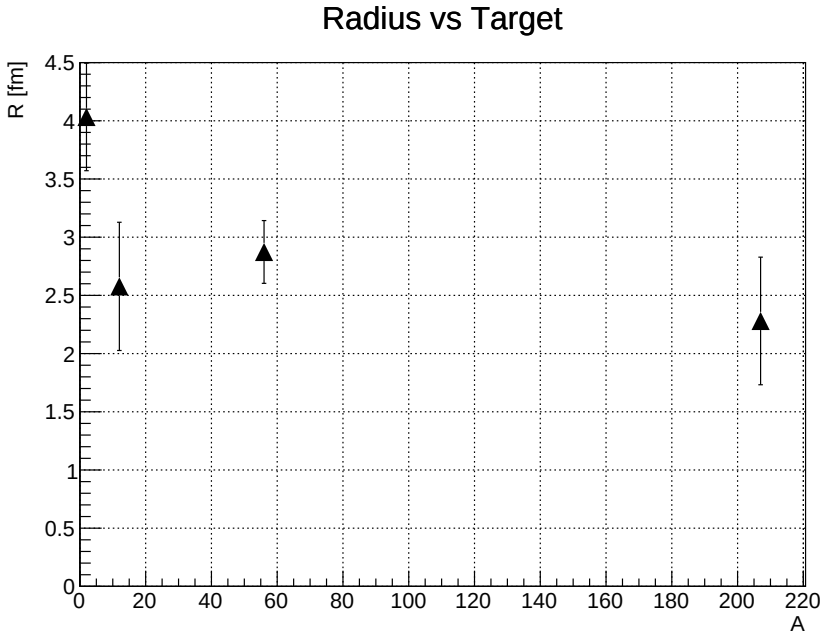

Figure 4.2: Source's measured Radius r vs nuclear mass number A. Nuclear target presented are: D2, C, Fe, Pb. This plot includes statistic and systematic errors.

4.2 Two Dimensional Study

Parameters obtained from Goldhaber fit of two-dimensional correlations, obtained in section 3.4, are shown in Table 4.2. In the two-dimensional case, the fit was performed in the range of $0.0 < q_l < 0.50$ GeV and of $0.0 < q_t < 0.50$ GeV; and λ, r_t and r_l are measured. In order to measure an elongation in the longitudinal direction of the pion source, we are interested in the ratio r_t/r_l.

We can clearly see that the pion source is elongated in the longitudinal direction among all targets.

4.2.1 Nuclear Target Comparison

The results obtained show no dependence in the longitudinal spatial component of the source r_l with a measurement of around 1.9 [fm] among solid targets. On the other hand, measured transverse radius r_t has a clear dependence on atomic number A. We

Target	r_t	r_l	r_t/r_l	λ
D2	$1.22 \pm 0.09 \pm 0.23$	$2.68 \pm 0.14 \pm 0.70$	$0.45 \pm 0.04 \pm 0.04$	$0.39 \pm 0.03 \pm 0.03$
C	$1.45 \pm 0.13 \pm 0.17$	$1.97 \pm 0.14 \pm 0.22$	$0.74 \pm 0.08 \pm 0.04$	$0.45 \pm 0.04 \pm 0.04$
Fe	$1.93 \pm 0.11 \pm 0.11$	$2.23 \pm 0.08 \pm 0.13$	$0.86 \pm 0.06 \pm 0.03$	$0.75 \pm 0.05 \pm 0.05$
Pb	$1.63 \pm 0.15 \pm 0.21$	$1.84 \pm 0.11 \pm 0.20$	$0.88 \pm 0.10 \pm 0.06$	$0.70 \pm 0.07 \pm 0.07$

Table 4.2: Parameters obtained from two-dimensional Goldhaber fit.

found that heavier nuclear targets present larger values of r_t.

This leads to the ratio between both spatial parameters r_t/r_l to increase with nuclear target number A as can be seen in Figure 4.4. This shows that the source region is elongated in all nuclear targets in the direction of the longitudinal axis. For light nuclei, the elongation is stronger and the elongation is diminished in heavier nuclei.

From Fig. 4.6, shows parameter λ in the two-dimensional case. Similar, but not exact same grade of coherence can be seen comparing one and two dimensional studies as seen in Fig.

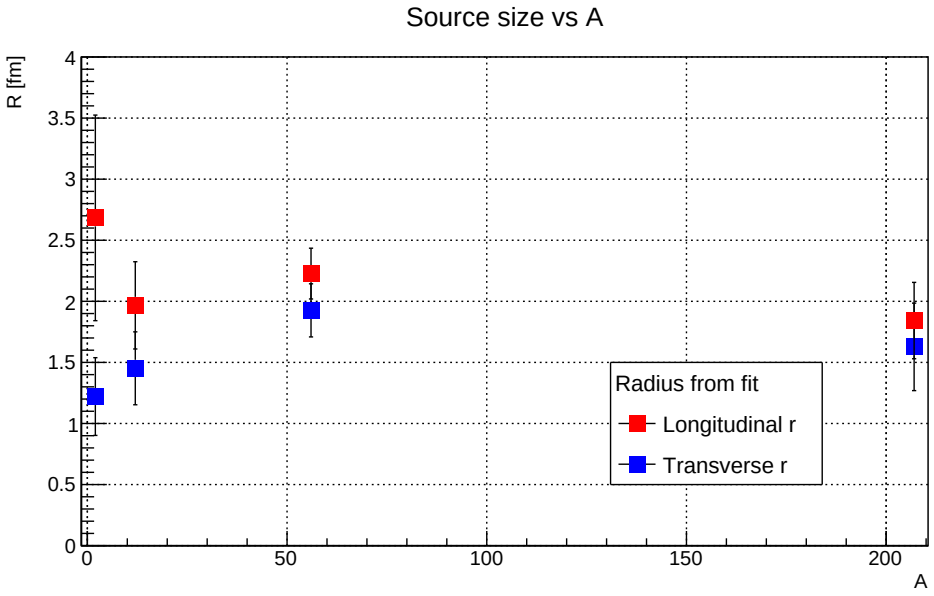

Figure 4.3: Source's spatial dimensions vs nuclear mass number A in two-dimensional study. Nuclear target presented are: D2, C, Fe, Pb. This plot includes statistic and systematic errors.

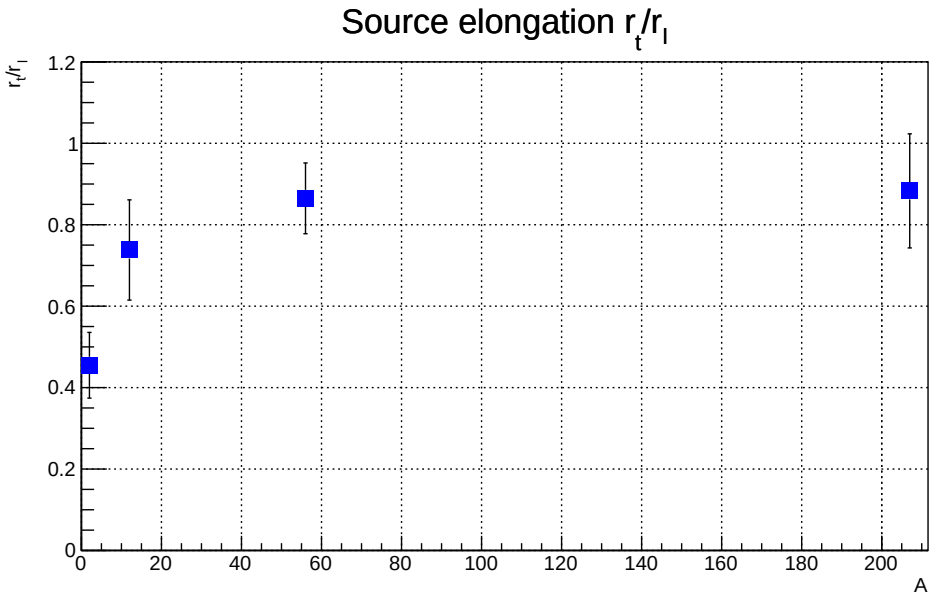

Figure 4.4: Source elongation vs nuclear mass number A.

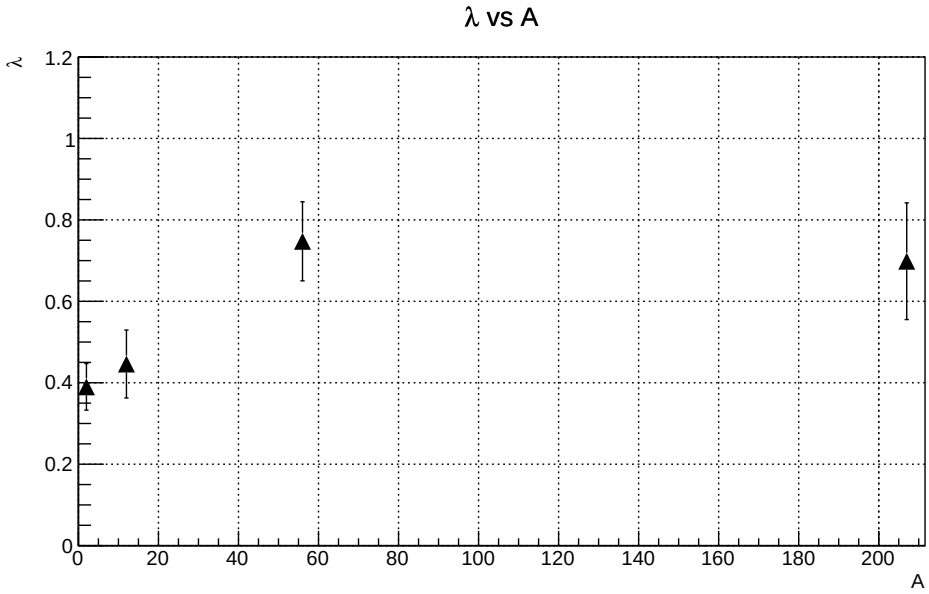

Figure 4.5: Coherence parameter λ vs Nucleus comparison in two-dimensional study. This plot includes statistic and systematic errors.

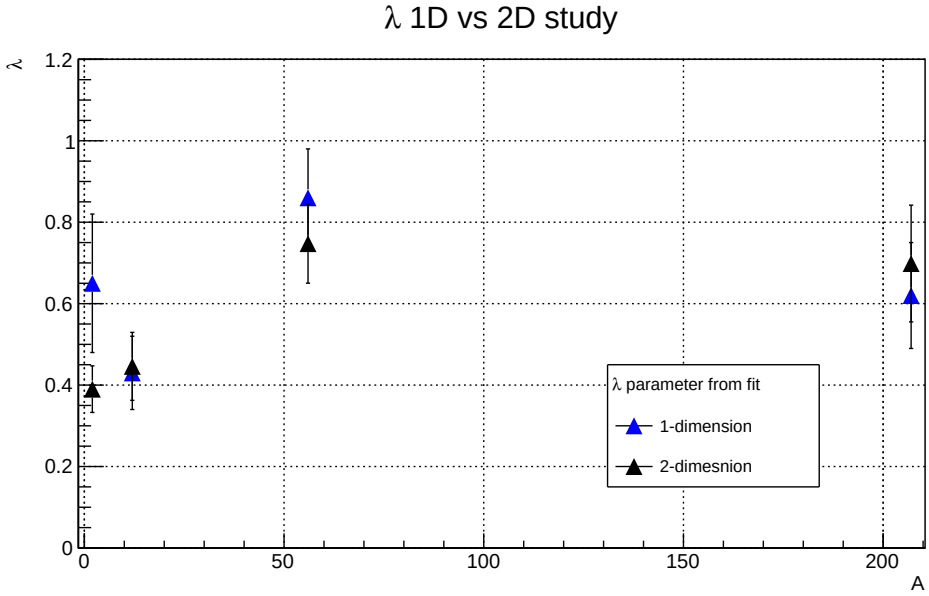

Figure 4.6: Coherence parameter λ vs Nucleus comparison in one and two-dimensional studies. This plot includes statistic and systematic errors.

Chapter 5

Conclusions and Future Analysis

From the plots shown in Fig.3.15, 3.16, 3.18, 3.20, and 3.22, we can clearly see that Bose-Einstein correlation were observed. The analysis was performed in one and two-dimensions with some minor differences found between them, regarding the degree of coherence of the source (λ).

From the one-dimensional study, we can conclude that the size of the pion source (r) was found to be the same, within errors, among solid targets: around 2.4 [fm]. Liquid target presents a bigger size of around 4 [fm].

From the two-dimensional study, we found elongation of the source along its longitudinal component ($r_t < r_l$) in all targets. The elongation is dependant of the nuclear medium and it is stronger for lighter targets ($r_t/r_l = 0.45$ for D2 compared to $r_t/r_l = 0.88$ for Pb). The transverse component r_t get bigger with heavier targets. In the contrary, the longitudinal component r_l gets smaller (Fig. 4.3). The difference between the size of these two parameters gets smaller for heavier nuclear targets.

We also found that this effect reach a saturation point for heavy targets such as Fe and Pb. This behaviour could come from the fact that the pion source is completely located within the nuclear medium in heavier targets. On the contrary, for light targets such as deuterium, part of the formation process occurs outside the nucleus.

This analysis can be expanded by including alternative ways of background distribution construction. As it was mentioned, instead of the event-mixing method, it is also possible to perform the same analysis using unlike-sign pairs. This could help to cross

check the results obtained with the current method used. It could be possible to study the dependence of Bose-Einstein correlations in different kinematic ranges, and look for possible dependence in Z_h or other kinematic variables.

Further theory studies can be conducted to explain the elongation process and how the nuclear medium impacts on it.

Bibliography

[1] R. HANBURY BROWN and R. Q. TWISS. "A Test of a New Type of Stellar Interferometer on Sirius". In: *Nature* 178.4541 (1956), pp. 1046–1048. ISSN: 1476-4687. DOI: 10.1038/1781046a0. URL: https://doi.org/10.1038/1781046a0.

[2] Gerson Goldhaber et al. "Pion-Pion Correlations in Antiproton Annihilation Events". In: *Phys. Rev. Lett.* 3 (4 1959), pp. 181–183. DOI: 10.1103/PhysRevLett.3.181. URL: https://link.aps.org/doi/10.1103/PhysRevLett.3.181.

[3] Gerson Goldhaber et al. "Influence of Bose-Einstein Statistics on the Antiproton-Proton Annihilation Process". In: *Phys. Rev.* 120 (1 1960), pp. 300–312. DOI: 10.1103/PhysRev.120.300. URL: https://link.aps.org/doi/10.1103/PhysRev.120.300.

[4] Andrzej Bialas, Wojciech Florkowski, and Kacper Zalewski. "Finite size of hadrons and Bose–Einstein correlations in pp collisions at 7 TeV". In: *Physics Letters B* 748 (2015), pp. 9 –12. ISSN: 0370-2693. DOI: https://doi.org/10.1016/j.physletb.2015.06.053. URL: http://www.sciencedirect.com/science/article/pii/S037026931500475X.

[5] A Kisiel. "Underlying event background in two-pion correlations in p + p Collisions at s = 0.9 and 7 TeV". In: *Physics of Particles and Nuclei Letters* 8 (Dec. 2011). DOI: 10.1134/S1547477111090202.

[6] Mate Csanad. “Femtoscopic results in Au+Au and p+p from PHENIX at RHIC”. In: (2011). DOI: 10.1134/S1547477111090123. eprint: arXiv:1101.2086.

[7] W. J. Metzger et al. “Parametrization of Bose-Einstein correlations and reconstruction of the source function in hadronic Z-boson decays using the L3 detector”. en. In: *Brazilian Journal of Physics* 37 (June 2007), pp. 689 –693. ISSN: 0103-9733. URL: http://www.scielo.br/scielo.php?script=sci_arttext&pid=S0103-97332007000500002&nrm=iso.

[8] K. Aamodt et al. “Two-pion Bose–Einstein correlations in central Pb–Pb collisions at sNN=2.76 TeV”. In: *Physics Letters B* 696.4 (2011), pp. 328 –337. ISSN: 0370-2693. DOI: https://doi.org/10.1016/j.physletb.2010.12.053. URL: http://www.sciencedirect.com/science/article/pii/S0370269310014565.

[9] B. Abelev et al. “Freeze-out radii extracted from three-pion cumulants in pp, p–Pb and Pb–Pb collisions at the LHC”. In: *Physics Letters B* 739 (2014), pp. 139 –151. ISSN: 0370-2693. DOI: https://doi.org/10.1016/j.physletb.2014.10.034. URL: http://www.sciencedirect.com/science/article/pii/S0370269314007576.

[10] Sunil Manohar Dogra. “Bose–Einstein correlation measurements at CMS”. In: *Nuclear Physics A* 931 (2014). QUARK MATTER 2014, pp. 1061 –1065. ISSN: 0375-9474. DOI: https://doi.org/10.1016/j.nuclphysa.2014.08.074. URL: http://www.sciencedirect.com/science/article/pii/S0375947414003340.

[11] E877 Collaboration et al. “Two-pion correlations in Au+Au collisions at 10.8 GeV/c per nucleon”. In: (1997). DOI: 10.1103/PhysRevLett.78.2916. eprint: arXiv:physics/9702008.

[12] W. A. Zajc et al. “Two-pion correlations in heavy ion collisions”. In: *Phys. Rev. C* 29 (6 1984), pp. 2173–2187. DOI: 10.1103/PhysRevC.29.2173. URL: https://link.aps.org/doi/10.1103/PhysRevC.29.2173.

[13] ZEUS Collaboration. “Bose-Einstein correlations in one and two dimensions in deep inelastic scattering”. In: (2003). DOI: 10.1016/j.physletb.2003.12.068. eprint: arXiv:hep-ex/0311030.

[14] HERMES Collaboration et al. *Bose-Einstein correlations in hadron-pairs from lepto-production on nuclei ranging from hydrogen to xenon*. 2015. eprint: arXiv:1505.03102.

[15] C. Adloff. “Bose-Einstein Correlations in Deep Inelastic ep Scattering at HERA”. In: (1997). DOI: 10.1007/s002880050486. eprint: arXiv:hep-ex/9705001.

[16] Ulrich Heinz and Barbara V. Jacak. “TWO-PARTICLECORRELATIONS INRELATIVISTICHEA IONCOLLISIONS”. In: *Annual Review of Nuclear and Particle Science* 49.1 (1999), 529–579. ISSN: 1545-4134. DOI: 10.1146/annurev.nucl.49.1.529. URL: http://dx.doi.org/10.1146/annurev.nucl.49.1.529.

[17] VA Korotkov et al. “Bose-Einstein correlations in neutrino and antineutrino interactions with nucleons”. In: *Zeitschrift für Physik C Particles and Fields* 60.1 (1993), pp. 37–51.

[18] Christian Dollfus. “Bose-Einstein Correlations in Deep Inelastic Scattering at HERA”. PhD thesis. Universität Zürich, 1996.

[19] M. G. Bowler. “Bose Einstein symmetrisation, coherence and chaos; with particular application to e+e- annihilation”. In: *Zeitschrift fuer Physik C, Particles and Fields* 29.4 (1985), pp. 617–629. ISSN: 0170-9739. URL: http://inis.iaea.org/search/search.aspx?orig_q=RN:17014994.

[20] Scott Pratt. “Coherence and Coulomb effects on pion interferometry”. In: *Phys. Rev. D* 33 (1 1986), pp. 72–79. DOI: 10.1103/PhysRevD.33.72. URL: https://link.aps.org/doi/10.1103/PhysRevD.33.72.

[21] M.G. Bowler. “Coulomb corrections to Bose-Einstein corrections have greatly exaggerated”. In: *Physics Letters B* 270.1 (1991), pp. 69 –74. ISSN: 0370-2693. DOI: https://doi.org/10.1016/0370-2693(91)91541-3.

URL: http://www.sciencedirect.com/science/article/pii/0370269391915413.

[22] B.A. Mecking et al. “The CEBAF large acceptance spectrometer (CLAS)”. In: *Nuclear Instruments and Methods in Physics Research Section A: Accelerators, Spectrometers, Detectors and Associated Equipment* 503.3 (2003), pp. 513 – 553. ISSN: 0168-9002. DOI: https://doi.org/10.1016/S0168-9002(03)01001-5. URL: http://www.sciencedirect.com/science/article/pii/S0168900203010015.

[23] M.D Mestayer et al. “The CLAS drift chamber system”. In: *Nuclear Instruments and Methods in Physics Research Section A: Accelerators, Spectrometers, Detectors and Associated Equipment* 449.1 (2000), pp. 81 –111. ISSN: 0168-9002. DOI: https://doi.org/10.1016/S0168-9002(00)00151-0. URL: http://www.sciencedirect.com/science/article/pii/S0168900200001510.

[24] G Adams et al. “The CLAS Cherenkov detector”. In: 465 (June 2001), pp. 414–427.

[25] E.S. Smith et al. “The time-of-flight system for CLAS”. In: 432 (Aug. 1999), pp. 265–298.

[26] M Amarian et al. “The CLAS forward electromagnetic calorimeter”. In: 460 (May 2001), pp. 239–265.

[27] H. Hakobyan et al. “A double-target system for precision measurements of nuclear medium effects”. In: *Nuclear Instruments and Methods in Physics Research Section A: Accelerators, Spectrometers, Detectors and Associated Equipment* 592.3 (2008), pp. 218 –223. ISSN: 0168-9002. DOI: https://doi.org/10.1016/j.nima.2008.04.055. URL: http://www.sciencedirect.com/science/article/pii/S0168900208006098.

[28] V. Blobel. “BOS: Bank Organization System. Dynamic Storage Organization with FORTRAN”. In: (1977).

[29] R. Brun and F. Rademakers. “ROOT: An object oriented data analysis framework”. In: *Nucl. Instrum. Meth.* A389 (1997), pp. 81–86. DOI: 10.1016/S0168-9002(97)00048-X.

[30] *Analyser*. URL: https://github.com/utfsm-eg2-data-analysis/Analyser.

[31] W.K. Brooks and H. Hakobyan. “Experimental Studies of Hadronization and Parton Propagation in the Space-Time Domain”. In: *Nuclear Physics A* 830.1 (2009). Quark Matter 2009, pp. 361c –368c. ISSN: 0375-9474. DOI: https://doi.org/10.1016/j.nuclphysa.2009.10.031. URL: http://www.sciencedirect.com/science/article/pii/S037594740900685X.

[32] A.Vlassov K.Mikhailov A.Stavinskiy. “Methods for Close-track Efficiency Study and its Application for CLAS”. In: (2002).

[33] ZEUS Collaboration and S. Chekanov. “Bose-Einstein Correlations of Charged and Neutral Kaons in Deep Inelastic Scattering at HERA”. In: (2007). DOI: 10.1016/j.physletb.2007.06.052. eprint: arXiv:0706.2538.

[34] B. Andersson et al. “Parton fragmentation and string dynamics”. In: *Physics Reports* 97.2 (1983), pp. 31 –145. ISSN: 0370-1573. DOI: https://doi.org/10.1016/0370-1573(83)90080-7. URL: http://www.sciencedirect.com/science/article/pii/0370157383900807.

[35] Bo Andersson and Markus Ringnér. “Bose-Einstein correlations in the Lund model”. In: *Nuclear Physics B* 513.3 (1998), pp. 627 –644. ISSN: 0550-3213. DOI: https://doi.org/10.1016/S0550-3213(97)00722-0. URL: http://www.sciencedirect.com/science/article/pii/S0550321397007220.